

From AI Weather Prediction to Infrastructure Resilience: A Correction–Downscaling Framework for Tropical Cyclone Impacts

You Wu¹, Zhenguo Wang², Naiyu Wang¹✉

¹ College of Civil Engineering and Architecture, Zhejiang University, Hangzhou 310058, China

² State Grid Zhejiang Electric Power Co., LTD. Electric power Research Institute China

✉ Correspondence: naiyuwang@zju.edu.cn

ABSTRACT: This paper addresses a missing capability in infrastructure resilience: turning fast, global AI weather forecasts into asset-scale, actionable risk. We introduce the AI-based Correction–Downscaling Framework (ACDF), which transforms coarse AI weather prediction (AIWP) into 500-m, unbiased wind fields and transmission tower/line failure probabilities for tropical cyclones. ACDF separates storm-scale bias correction from terrain-aware downscaling, preventing error propagation while restoring sub-kilometer variability that governs structural loading. Tested on 11 typhoons affecting Zhejiang, China under leave-one-storm-out evaluation, ACDF reduces station-scale wind-speed MAE by 38.8% versus Pangu-Weather, matches observation-assimilated mesoscale analyses, yet runs in ~25 s per 12-h cycle on a single GPU. In the Typhoon Hagupit case, ACDF reproduced observed high-wind tails, isolated a coastal high-risk corridor, and flagged the line that failed, demonstrating actionable guidance at tower and line scales. ACDF provides an end-to-end pathway from AI global forecasts to operational, impact-based early warning for critical infrastructure.

KEY WORDS: Tropical cyclones; Real-time impact forecasts; Downscaling; Infrastructure resilience; Risk prediction; Deep learning

1 Introduction

Tropical cyclones (TCs) are among the most destructive natural hazards, repeatedly disrupting power, transport, and other lifeline systems (Esmalian et al., 2022; Roy et al., 2020; Yang et al., 2025). This paper addresses a missing capability at the heart of civil infrastructure resilience: turning fast, global AI weather forecasts into real-time, sub-kilometer, unbiased wind fields and asset-level failure probabilities that operators can act on. Rather than proposing a new AI forecast architecture, we bridge state-of-the-art AI-based weather prediction (AIWP) with infrastructure risk forecasting, delivering actionable early warning to support resilience planning with operational lead time.

TCs caused more than \$1.4 trillion in global economic losses between 1970 and 2019 (representing 38% of all disaster damages; WMO, 2021), with annual losses now exceeding \$100 billion and repeatedly disrupting critical infrastructure across coastal regions (China Power, 2019; NOAA, 2019; U.S. DOE, 2018). While AIWP research has been motivated and evaluated largely within the meteorological community—where success is measured in

track accuracy, intensity skill, or medium-range lead time (Bauer et al., 2015; Lam et al., 2023; Bi et al., 2023; Chen et al., 2023; Allen et al., 2025; Price et al., 2025)—these products remain poorly aligned with the needs of infrastructure risk management (Reichstein et al., 2025; Huang & Wang, 2025, 2024; Ti et al., 2022; Wu et al., 2025). Mitigating losses in spatially distributed systems such as power grids and transportation networks requires more than forecasts of track or peak intensity. It demands insights into when, where, and with what probability critical assets might fail, and how localized failures propagate into system-level impact—i.e., impact-based forecasting (Coughlan De Perez et al., 2016; WMO, 2021; Harrowsmith et al., 2020; Huang & Wang, 2024; Cui et al., 2025). This shift from hazard-oriented early warning to infrastructure-aware, impact-based intelligence is increasingly recognized as essential for climate resilience.

Meeting this need requires three capabilities to be satisfied simultaneously in meteorological forecasts: high resolution (sub-kilometer detail to capture terrain-modulated wind variability that governs localized structural loading), scalability (regional coverage to support network-level risk assessments), and computational efficiency (Low-latency

inference for real-time decision-making during rapidly evolving TCs).

Physics-based Numerical Weather Prediction (NWP) models struggle to deliver all three. Global systems such as the ECMWF integrated forecasting system (ECMWF-IFS) and the NCEP Global Forecast System (GFS) operate at 9–25 km grid spacing, while even regional systems like High-Resolution Rapid Refresh (HRRR) remain limited to ~3 km—still insufficient for asset-level risk assessment in complex terrain. The Weather Research and Forecasting (WRF) model can achieve <1 km resolution (Skamarock et al., 2019; Perini De Souza et al., 2022), but its computational demands prohibit real-time deployment. Moreover, NWP

forecasts often exhibit systematic errors in intensity and storm structure (Rasp et al., 2024; Olivetti & Messori, 2024).

Emerging AIWP models such as GraphCast, Pangu-Weather, Fuxi, Aardvark, and GenCast (Lam et al., 2023; Bi et al., 2023; Chen et al., 2023; Allen et al., 2025; Price et al., 2025) deliver orders-of-magnitude faster inference and competitive medium-range skill. Yet they inherit the coarse resolution and structural biases of their training reanalyses (e.g., ERA5 at ~25 km), limiting their ability to resolve local wind extremes and leading to persistent intensity underestimation (Rasp et al., 2024; Olivetti and Messori, 2024).

Table 1. Literature gap summary: wind forecast correction & downscaling.

Category	Study / Approach	Real-Time Correction	Terrain-Aware Downscaling	Resolution Achieved	Regional Scale (>10 ⁵ km ²)
Site-specific	Ding et al. (2019); Lim et al. (2022); Wu et al. (2025)	√	×	Site scale	×
Continuous field	Huang et al. (2024)	√	×	25 km	√ Global
	Wu et al. (2024)	√	×	3 km	√ Regional (but no terrain)
	Xiang et al. (2024)	√	×	3 km	√ CONUS
	Liu et al. (2025)	×	×	25 km	√ Global archive
	Guo et al. (2025)	√	×	25 km	√ Global
Label-free	Han et al. (2024)	×	√	9 km	√ Global
	Liu et al. (2025)	×	√	3 km	√ Partial CONUS
Label-dependent	Liu et al. (2024)	×	√	25 km	√ ERA5 label
	Zhong et al. (2024)	×	√	1 km	√ HRCLDAS label
	Mardani et al. (2025)	×	×	2 km	√ WRF label without terrain input
	Lockwood et al. (2024)	×	×	6 km	×
	This study (ACDF)	√	√	500 m	√
		Real-time assimilation	High-resolution terrain-aware		Regional-scale (>10⁵ km², infrastructure networks)

Challenge: Systematic bias and coarse spatial resolution in global AI forecasts

Aim: Impact-based early-warning for infrastructural risk mitigation and resilience planning

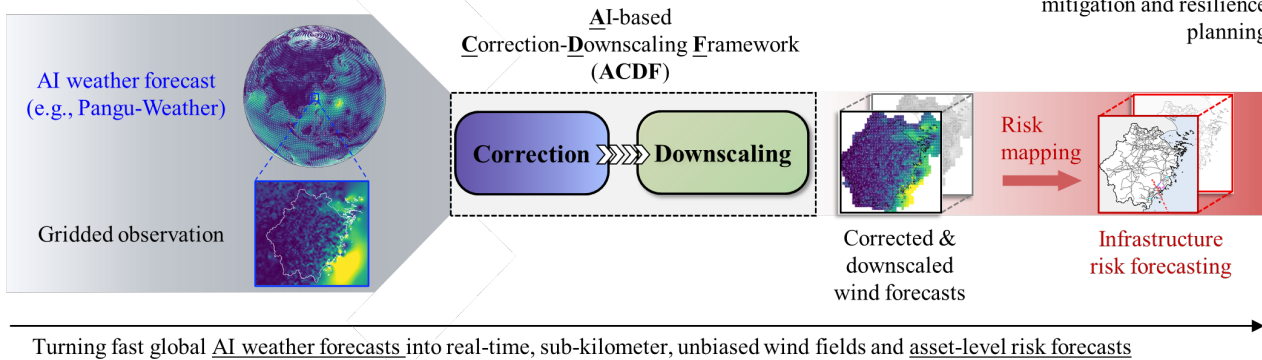


Fig. 1. Conceptual overview of the proposed AI-based Correction-Downscaling Framework (ACDF).

Recent research has advanced two complementary directions. Correction methods use observations to reduce intensity biases, either through site-specific assimilation (Ding et al., 2019; Lim et al., 2022; Wu et al., 2025) or spatially continuous approaches using GNNs, Transformers, or diffusion models (Wu, et al., 2023; Huang et al., 2024; Wu et al., 2024; Xiang et al., 2024; Liu et al., 2025; Guo et al., 2025). While these approaches improve large-scale coherence, they typically operate at coarse native and lack terrain awareness. Downscaling methods, by contrast, reconstruct high-resolution fields from coarse inputs. Label-free strategies (Han et al., 2024; Liu et al., 2025) rely only on low-resolution priors and cannot resolve micro-scale terrain effects, while label-dependent methods (Liu et al., 2024; Zhong et al., 2024; Lockwood et al. 2024; Mardani et al., 2025) learn from paired coarse-fine datasets or WRF-generated high-resolution labels. Yet these remain tied to static training data and do not integrate real-time corrections.

Table 1 synthesizes this landscape, contrasting recent advances in TC wind field correction and downscaling across real-time applicability, terrain awareness, resolution, and scalability. Correction methods reduce storm-scale biases but neglect fine-scale variability, while downscaling methods add spatial detail but assume error-free inputs. No existing framework jointly achieves real-time correction, terrain-aware downscaling, and province-scale deployment.

This gap is consequential for civil engineering. On one side, AIWP now produces global forecasts in minutes rather than hours, rivaling or surpassing NWP in speed and accuracy. On the other, civil infrastructure systems still lack impact-based risk forecasts—unbiased, high-resolution wind fields coupled to fragility models that predict which assets will fail and when. The result is an implementation gap: fast, powerful AI forecasts exist, but infrastructure communities still lack the means to convert them into actionable risk intelligence for resilience planning.

This study directly bridges that gap. We introduce the AI-based Correction-Downscaling Framework (ACDF), a modular, interpretable system that processes raw AIWP outputs into 500 m, province-scale, near-real-time wind fields and couples them to fragility models to produce asset-level failure probabilities. ACDF decouples storm-scale bias correction from terrain-aware downscaling, preventing error propagation and aligning forecasts with infrastructure needs. Figure 1 provides a conceptual overview, and the main contributions of this study are as follows:

- **Bridging AI weather prediction and infrastructure risk forecasting.** We present, to our knowledge, the first framework that translates state-of-the-art AI forecasts into real-time, infrastructure-specific risk predictions. Unlike prior AIWP work focused on track or intensity, ACDF targets fragility-informed failure probabilities of power transmission systems under TCs.
- **A modular correction-downscaling architecture.** ACDF decouples storm-scale bias correction from terrain-aware downscaling, improving interpretability, mitigating error propagation, and addressing both large-scale displacement errors and fine-scale terrain effects.
- **Province-scale, high-resolution, validated performance.** ACDF processes AIWP forecasts to produce 500 m wind field forecasts over domains exceeding 100,000 km² within seconds. In Leave-One-Storm-Out (LOSO) cross-validation on 11 TCs, ACDF achieves a 38.8% MAE reduction vs. Pangu-Weather (selected bench-mark AIWP) forecasts, with consistent gains in high-wind and complex-terrain conditions.
- **End-to-end infrastructure risk forecast demonstration.** In Zhejiang’s grid during Typhoon Hagupit (2020), ACDF generated transmission-line-specific failure probability forecasts with lead times up to 12 h that aligned with observed post-event damage and outperformed risk forecasts derived directly from raw

AIWP inputs, demonstrating actionable lead time for proactive operations.

ACDF’s ability to convert global forecasts into risk intelligence within seconds opens the possibility of delivering impact-based early warnings that save lives and reduce economic losses by enabling targeted evacuations, proactive grid operations, and pre-event resource allocation. To our knowledge, this represents an early demonstration of an end-to-end framework coupling AIWP with risk forecasting for civil infrastructure system at regional scale under tropical cyclones.

2 Formulation of AI-based Correction–Downscaling Framework (ACDF)

From an engineering standpoint, bridging the gap between coarse atmospheric forecasts and infrastructure-scale hazard prediction requires a framework that is both physically interpretable and data-efficient. The AI-based Correction–Downscaling Framework (ACDF) operationalizes this goal through a two-module spatiotemporal learning design that:

1. Assimilates AIWP forecasts and gridded analyses, with high-fidelity station observations used as supervisory labels, so that all available information contributes to forecast refinement;
2. Corrects large-scale, systematic errors in TC intensity and wind structure; and
3. Reconstructs sub-kilometer wind variability driven by static terrain features such as elevation and land cover, which critically govern localized loading on infrastructure assets.

By explicitly decoupling downscaling from correction, ACDF ensures that storm-scale biases are removed before terrain-induced refinements are added, preventing error propagation and yielding hazard forecasts that are dynamically consistent, geographically realistic, and directly usable for infrastructure risk assessment.

2.1 Notation

Table 2 summarizes the primary symbols used in this section. These notations define the inputs, outputs, and intermediate representations of the ACDF.

2.2 Problem formulation

ACDF addresses TC wind forecasting using Pangu-Weather (Bi et al., 2023) as the primary source of coarse-resolution inputs. Given coarse forecasts $\mathbf{X}_{\text{pangu}}$, historical gridded observations $\mathbf{X}_{\text{LR-obs}}$, station observation data $\mathbf{Y}_{\text{ST-obs}}$, and static terrain features $\mathbf{X}_{\text{terrain}}$ (notations summarized in Table 2), the framework learns to produce high-resolution

forecasts $\hat{\mathbf{Y}}_{\text{ds}}$.

The learning task is formalized as a composite mapping:

$$\hat{\mathbf{Y}}_{\text{ds}} = \mathcal{F}_2(\mathcal{F}_1(\mathbf{X}_{\text{pangu}}, \mathbf{X}_{\text{LR-obs}}; \theta_1), \mathbf{X}_{\text{terrain}}; \theta_2) \quad (1)$$

Here, \mathcal{F}_1 module performs bias correction, generating a coarse corrected field $\hat{\mathbf{X}}_{\text{corr}}$. \mathcal{F}_2 module applies terrain-aware downscaling, producing the final 500 m-resolution forecast $\hat{\mathbf{Y}}_{\text{ds}}$.

Physically, \mathcal{F}_1 removes TC-scale biases (e.g., intensity misestimation and structure misforecast), while \mathcal{F}_2 superimposes localized terrain effects (e.g., ridge speed-up and valley sheltering). This decoupled design enables each module to be independently trained and optimized, ensuring that the final wind field is both dynamically consistent and geographically realistic. Notably, it also allows flexible integration with different upstream forecast models and downstream infrastructure risk assessment workflows.

2.3 Correction module (\mathcal{F}_1): real-time bias adjustment

The correction module adjusts raw Pangu forecasts so that they remain consistent with the evolving observed atmospheric state. This step is essential because even state-of-the-art AIWP and NWP models can exhibit systematic biases.

We implement \mathcal{F}_1 as a graph-based neural network that processes both the H -hour historical segments of $\mathbf{X}_{\text{pangu}}$ and $\mathbf{X}_{\text{LR-obs}}$, together with the τ -hour future forecast segments from $\mathbf{X}_{\text{pangu}}$. This sequential encoding captures temporal dependencies and systematic forecast–observation discrepancies between forecasts and observations:

$$\hat{\mathbf{X}}_{\text{corr}} = \mathcal{F}_1(\mathbf{X}_{\text{pangu}}, \mathbf{X}_{\text{LR-obs}}), \hat{\mathbf{X}}_{\text{corr}} \in \mathbb{R}^{\tau \times N \times 2} \quad (2)$$

The output is a bias-corrected wind field at the original coarse resolution. By aligning large-scale circulation with recent observations, $\hat{\mathbf{X}}_{\text{corr}}$ serves as a dynamically consistent input for terrain-aware refinement in downscaling module.

2.4 Downscaling module (\mathcal{F}_2): terrain-aware spatial refinement

The second module addresses the inherent scale limitation: even bias-corrected coarse forecasts cannot resolve sub-kilometer wind variability in complex terrain. Features such as steep ridges, narrow valleys, and coastal headlands can locally accelerate or suppress winds, with major implications for infrastructure exposure.

We implement \mathcal{F}_2 as a hierarchical encoder-decoder trained on paired coarse wind fields and high-resolution labels generated from offline WRF simulations. Its inputs are the bias-corrected coarse forecast $\hat{\mathbf{X}}_{\text{corr}}$ and high-resolution static terrain maps $\mathbf{X}_{\text{terrain}}$:

Table 2. Notation for the ACDF framework.

Symbol	Dimension	Description
$\mathbf{X}_{\text{pangu}}$	$\mathbb{R}^{(H+\tau) \times N \times 2}$	Coarse-resolution forecasts from Pangu-Weather, including H hours of history and τ -hour lead forecasts at N grid nodes; last dimension: zonal (U) and meridional (V) wind components.
$\mathbf{X}_{\text{LR-obs}}$	$\mathbb{R}^{H \times N \times 2}$	Historical low-resolution wind observations (i.e., HRCLDAS) aligned with the Pangu-Weather grid. (Historical inputs used jointly with forecasts)
$\mathbf{Y}_{\text{LR-obs}}$	$\mathbb{R}^{\tau \times N \times 2}$	Low-resolution grid observations over the forecast period, used as training targets. (Future observations used for supervision)
$\mathbf{Y}_{\text{ST-obs}}$	$\mathbb{R}^{\tau \times S \times 2}$	Station observations at S locations, providing state-based high-fidelity ground truth (used in validation and training supervision).
$\mathbf{X}_{\text{terrain}}$	$\mathbb{R}^{H' \times W' \times 2}$	High-resolution static terrain features (e.g., elevation, land cover) at 500 m resolution, with spatial dimensions H' and W' .
$\hat{\mathbf{X}}_{\text{corr}}$	$\mathbb{R}^{\tau \times N \times 2}$	Bias-corrected coarse wind field produced by Stage 1.
$\hat{\mathbf{Y}}_{\text{ds}}$	$\mathbb{R}^{\tau \times H' \times W' \times 2}$	Bias-corrected and downscaled wind field at 500 m resolution.
$\mathcal{F}_1(\cdot; \theta_1)$	—	Bias correction module, parameterized by θ_1 .
$\mathcal{F}_2(\cdot; \theta_2)$	—	Terrain-aware downscaling module, parameterized by θ_2 .
H	—	Number of historical hours.
τ	—	Forecast lead time (hours).
N	—	Number of coarse grid nodes.
S	—	Number of weather stations.
i	—	Downscaling patch index.
n	—	Divided n patches in the d03 region for downscaling.
H', W'	—	Spatial dimensions of the high-resolution domain (500 m resolution).

$$\hat{\mathbf{Y}}_{\text{ds}} = \mathcal{F}_2(\hat{\mathbf{X}}_{\text{corr}}, \mathbf{X}_{\text{terrain}}), \hat{\mathbf{Y}}_{\text{ds}} \in \mathbb{R}^{\tau \times H' \times W' \times 2} \quad (3)$$

A residual learning formulation is adopted so that the large-scale flow structures in $\hat{\mathbf{X}}_{\text{corr}}$ are preserved, while \mathcal{F}_2 focuses exclusively on reconstructing terrain-induced perturbations. This design ensures that the downscaled forecasts remain physically plausible, geographically realistic, and directly relevant for infrastructure-scale risk assessment.

2.5 Sequential training strategy

To maximize the complementary strengths of the two stages, ACDF adopts a sequential, dependency-aware two-stage training scheme. The overall workflow is illustrated in Figure 2, which highlights how bias correction and terrain-aware downscaling are trained in sequence. This design reflects the distinct physical and statistical roles of each module.

Stage 1 Pre-train downscaling module (\mathcal{F}_2)

- The downscaling module is trained first using paired coarse-resolution and high-resolution wind fields generated by offline WRF simulations.

- This stage focuses on learning fine-scale, terrain-driven perturbations that are additive to large-scale flow patterns.

- Pre-training in isolation ensures that \mathcal{F}_2 develops a stable, domain-general mapping of terrain effects, independent of upstream forecast biases.

Stage 2 Train correction module (\mathcal{F}_1) with parameter-frozen downscaling

- Once \mathcal{F}_2 is trained, its parameters θ_2 are frozen.
- The bias correction module \mathcal{F}_1 is then trained with \mathcal{F}_2 appended, so that coarse-scale bias adjustments are directly optimized for their impact on the final high-resolution forecasts $\hat{\mathbf{Y}}_{\text{ds}}$. Because the residual design preserves large-scale flow fields inherited from $\hat{\mathbf{X}}_{\text{corr}}$ (Section 2.4), \mathcal{F}_2 trained on WRF-driven coarse-fine pairs generalizes well to corrected Pangu fields during joint training.

- This dependency-aware strategy prevents systematic errors in storm-scale forecasts from propagating into terrain-refined outputs, as shown in Figure 2.

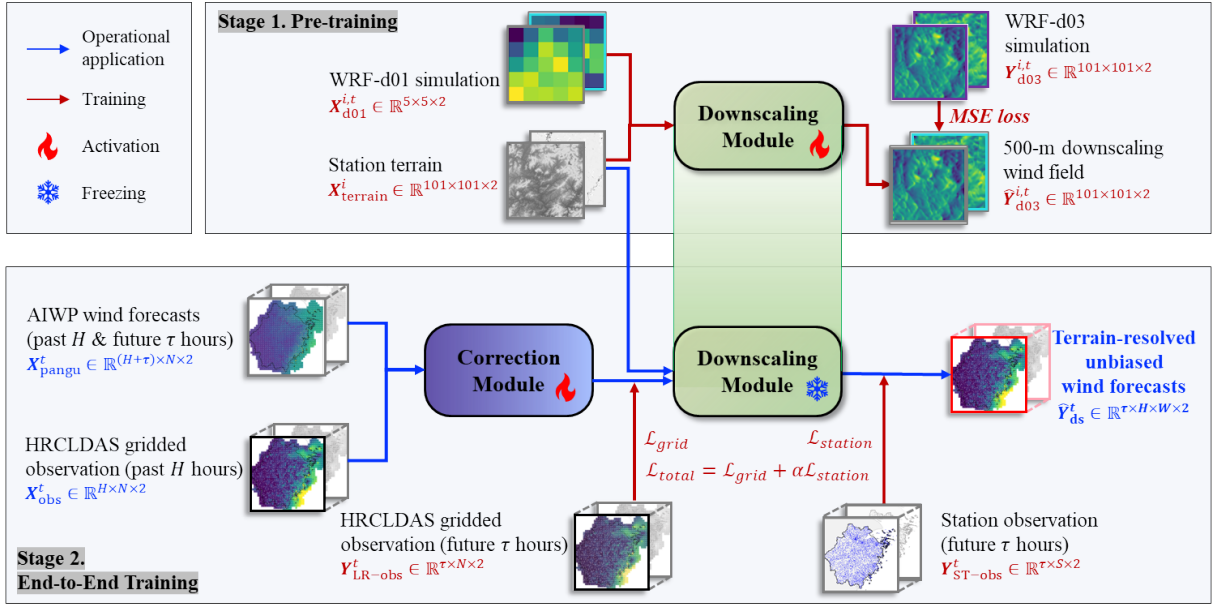


Fig. 2. Sequential training strategy of the ACDF.

This sequential design operationalizes the core novelty introduced in Section 1: decoupling storm-scale bias removal from terrain-driven. By training the two modules in sequence, ACDF prevents storm-scale errors from contaminating terrain-resolved fields, ensuring forecasts that remain operationally robust, physically interpretable, and directly applicable to infrastructure risk assessment.

3 Data and Preprocessing

Bridging the gap between coarse atmospheric forecasts and infrastructure-scale hazard prediction requires datasets that reflect both storm-scale dynamics and fine-scale terrain effects. To meet this need, we assemble a multi-source dataset that integrates AIWP forecasts, mesoscale numerical simulations, gridded analyses, ground-based observations and static terrain features. Together, these heterogeneous sources serve two complementary roles: (i) enabling the correction module to reduce systematic forecast biases by anchoring predictions to recent observations, and (ii) allowing the downscaling module to reconstruct physically plausible sub-kilometer wind variability shaped by topography. The study area is Zhejiang Province, China—a coastal region with complex terrain and frequent TC exposure, making it an ideal testbed.

3.1 Data sources and event set

This study leverages 11 TCs that impacted Zhejiang Province between 2012 and 2022, covering diverse range of tracks and intensities (Figure 3). These events align with ACDF’s two-module design: Five severe TCs with high-fidelity WRF simulations form Group A, supplying paired

coarse–fine training data for the downscaling module. All 11 events, including both Groups A and B, contribute forecasts and observations for training the correction module (Table 3). This dual structure ensures both broad event coverage and the high-resolution supervision needed to capture terrain-driven variability.

AIWP forecasts (Pangu-Weather): Hourly 10-m wind forecasts from Pangu-Weather (Bi et al., 2023) provide the coarse, biased inputs that ACDF is designed to refine. The native 0.25° forecasts are bilinearly resampled to a 0.125° (~ 12.5 km) grid with N nodes, forming tensors $\mathbf{X}_{\text{pangu}}^t \in \mathbb{R}^{N \times 2}$ that contain zonal (U) and meridional (V) wind components. To remain consistent with Pangu-Weather’s training baseline, ERA5-driven reforecasts are used in this study, while an operational setting would substitute real-time GFS-driven forecasts.

High-resolution WRF simulations: Training data for terrain-aware downscaling are supplied by nested WRF simulations of the five Group A TCs. Three domains were configured: d01 at 12.5 km, d02 at 2.5 km, and d03 at 500 m over Zhejiang Province (Figure 4a). Samples from d01 ($\mathbf{X}_{\text{d01}}^t$, 12.5 km) and d03 ($\mathbf{X}_{\text{d03}}^t$, 500 m) provide physically consistent coarse–fine pairs, where d01 provides the baseline coarse fields (Figure 4c) and d03 provides terrain-resolved labels (Figure 4e) of how topography modulates TC wind structure. Compared with observation-interpolated wind fields from sparse meteorological stations, the WRF simulations (Figures 4(c-e)) provide dense, coherent supervision across the full domain.

HRCLDAS gridded analyses: The HRCLDAS product (Han et al., 2020) provides hourly 1-km wind analyses across mainland China. For ACDF, these fields are aggregated to

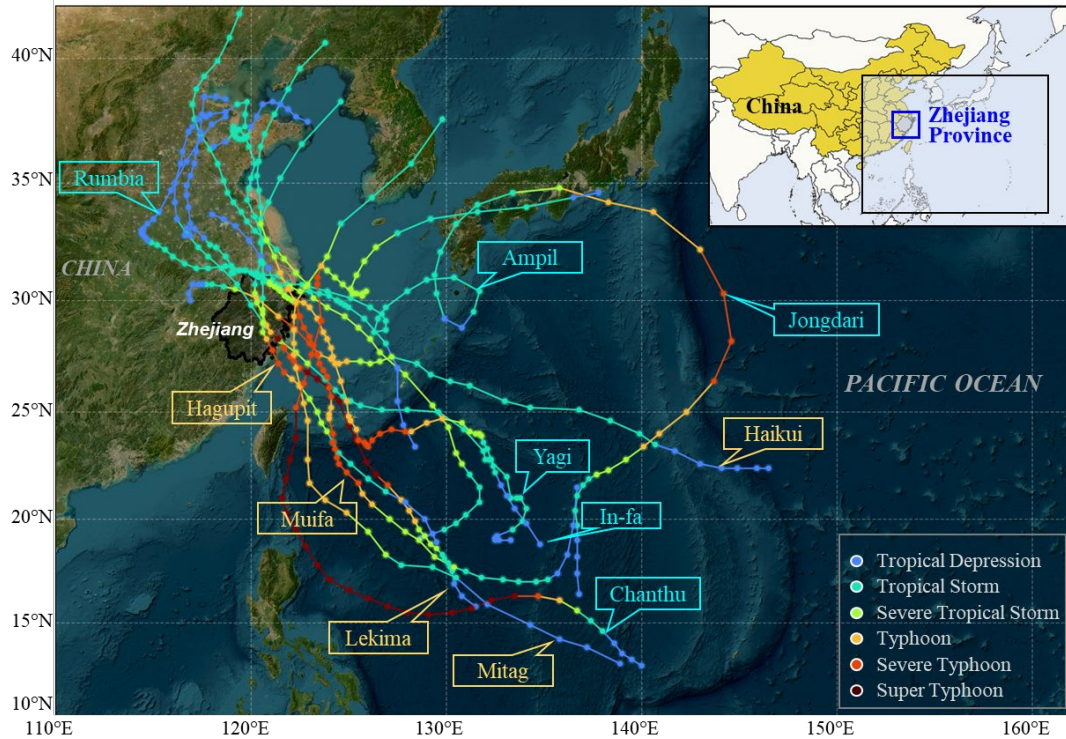


Fig. 3. Total 11 TC events used for model development and validation and 5 severe events (in yellow) selected for WRF simulations.

12.5 km (as in Figure 4g) to align with Pangu’s processed grid. HRCLDAS plays two complementary roles: supplying historical inputs (X_{LR-obs}) to characterize forecast biases, and providing spatially continuous labels (Y_{LR-obs}) for training the correction module.

Ground station observations: Hourly, 2-min averaged winds from 2,513 stations across Zhejiang Province (Figure 4f) offer high-fidelity, point-scale labels ($Y_{ST-obs}^t \in \mathbb{R}^{S \times 2}$). Unlike gridded analyses, which are spatially smoothed, station records directly anchor forecasts at infrastructure-relevant locations, making them indispensable for operational risk assessment.

Static terrain features: Elevation data from the 30-m ASTER DEM (Abrams et al., 2020) and land cover classifications are resampled to the 500-m grid of the d03 domain. As shown in Figure 4b, the mountainous and coastal landforms strongly influence wind acceleration and sheltering. These terrain datasets, encoded as invariant conditioning features ($X_{terrain}$), enable the downscaling module to generalize terrain-induced wind perturbations across diverse TC events.

3.2 Preprocessing pipeline

The preprocessing pipeline harmonizes these heterogeneous sources into structured training samples tailored to ACDF’s two modules. Its design serves two main goals: (1) aligning spatiotemporal resolutions with the learning objectives of each module, and (2) enabling rigorous evaluation of generalization on unseen storms. Dataset usage is summarized in Table 4.

Preprint. Under Review.

Cross-validation and partitioning: ACDF is trained and validated under a leave-one-storm-out (LOSO) protocol. In each fold, one of the five Group A WRF-simulated TCs—Haikui (2012), Lekima (2019), Mitag (2019), Hagupit (2020), or Muifa (2022)—is withheld for testing, while the remaining events are split into training (85%) and validation (15%) sets. This design maximizes use of limited events while ensuring evaluation under previously unseen tracks, intensities, and terrain interactions. The Hagupit case study (Section 6) corresponds to the fold in which Hagupit was withheld, providing a strict out-of-sample test.

Downscaling module pre-training: The downscaling task is posed as a spatial super-resolution problem, requiring paired coarse–fine wind fields that explicitly resolve terrain effects. For each timestep t in the Group A storms, overlapping patches are extracted from d01 (12.5 km) and paired with d03 (500 m) outputs. Each coarse input patch ($X_{d01}^{i,t} \in \mathbb{R}^{5 \times 5 \times 2}$) is matched with its corresponding fine-resolution label ($X_{d03}^{i,t} \in \mathbb{R}^{101 \times 101 \times 2}$) and concatenated with a terrain patch ($X_{terrain}^i \in \mathbb{R}^{101 \times 101 \times 2}$). Using a patch size of $0.5^\circ \times 0.5^\circ$ and a stride of 0.25° , this procedure yields 35,028 coarse–fine sample pairs. The large sample count arises from patch extraction across both space and time, ensuring dense, physically consistent supervision for terrain-aware refinement.

Correction module end-to-end training: The correction task is formulated as a spatiotemporal sequence-to-sequence problem. Using all 11 TCs, sliding windows of $(H + \tau)$ hours are constructed, consisting of H hours of historical data and

Table 3. TC datasets for model development.

ID	Name	Data Type	Time Span (UTC)	Spatial Coverage*	Notation
Group A:				Used in	
Events with WRF Simulation + Forecast & Observation				Correction & Downscaling Modules	
1211	Haikui	WRF simulation	2012/08/07/01 – 2012/08/08/18		
		Forecast & Obs	2012/08/04/01 – 2012/08/08/15		
1909	Lekima	WRF simulation	2019/08/09/07 – 2019/08/10/16		
		Forecast & Obs	2019/08/07/01 – 2019/08/10/15		
1918	Mitag	WRF simulation	2019/09/30/13 – 2019/10/01/21	d01, d02, d03	$X_{d01}^t, X_{d03}^t,$
		Forecast & Obs	2019/09/29/13 – 2019/10/02/15	& Study region	$X_{pangu}^t, X_{LR-obs}^t,$
2004	Hagupit	WRF simulation	2020/08/03/07 – 2020/08/04/12		$Y_{LR-obs}^t, Y_{ST-obs}^t$
		Forecast & Obs	2020/08/01/16 – 2020/08/05/14		
2212	Muifa	WRF simulation	2022/09/13/19 – 2022/09/14/18		
		Forecast & Obs	2022/09/12/11 – 2022/09/14/23		
Group B:				Used in	
Events with Forecast & Observation Only				Correction Module	
1810	Ampil		2018/07/20/23 – 2018/07/22/10		
1812	Jongdari		2018/08/01/23 – 2018/08/03/10		
1814	Yagi	Forecast & Obs	2018/08/11/16 – 2018/08/13/10	Study region	$X_{pangu}^t, X_{LR-obs}^t,$
1818	Rumbia		2018/08/15/00 – 2018/08/17/10		$Y_{LR-obs}^t, Y_{ST-obs}^t$
2106	In-fa		2021/07/23/11 – 2021/07/26/15		
2114	Chanthu		2021/09/12/11 – 2021/09/14/15		

* The spatial coverage: d01: 83.91°E–146.09°E & 12.14°N–45.64°N; d02: 116.76°E–123.98°E & 26.06°N–32.24°N; d03: 117.65°E–122.99°E & 26.97°N–31.33°N; Study region: 117.875°E–122.625°E & 27.25°N–31.00°N.

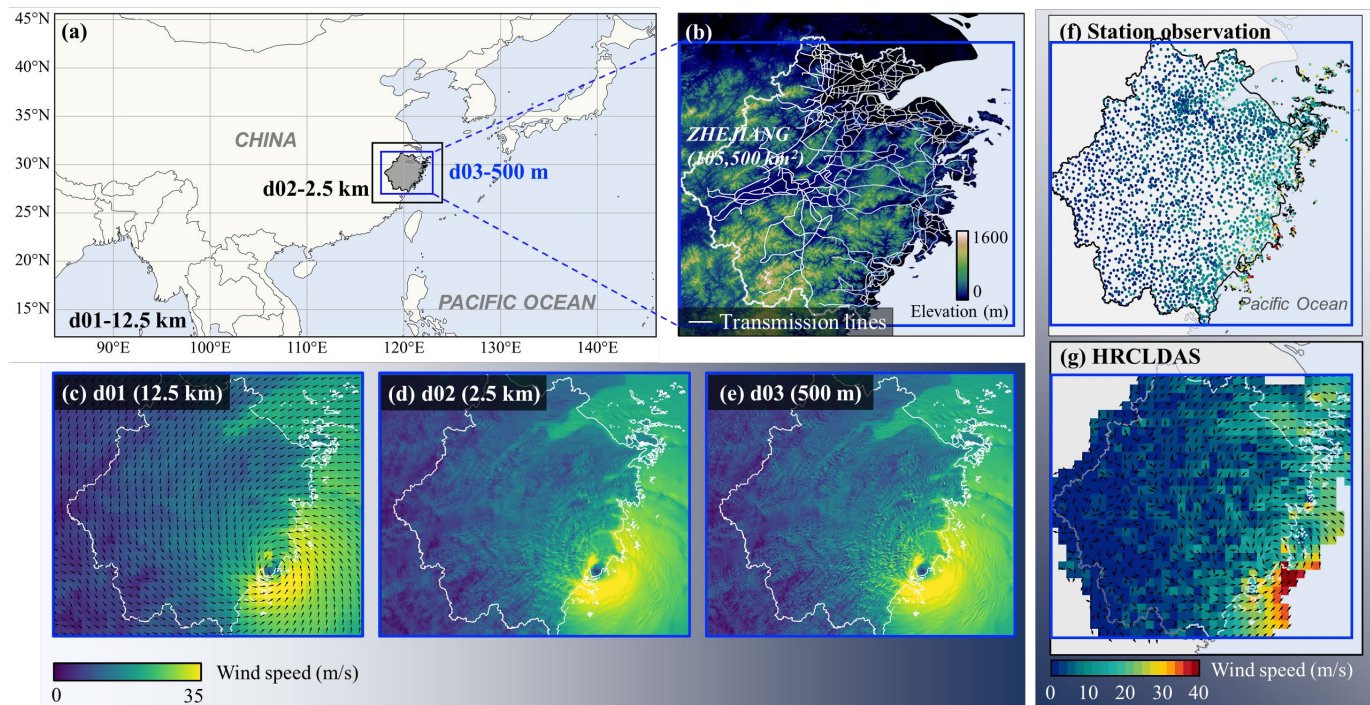


Fig. 4. Overview of the study domain and datasets: (a) nested WRF simulation domains (d01: 12.5 km, d02: 2.5 km, d03: 500 m) centered on Zhejiang Province; (b) digital elevation model (DEM) overlaid with the provincial transmission grid; (c-e) d01, d02 and d03 wind field simulations for 2019/08/09/18 UTC; (f) spatial distribution of 2,513 ground weather stations; and (g) Computational domain constrained by station coverage using HRCLDAS wind fields (illustrated with winds at 2019/08/09/18 UTC as an example).

Table 4. Preprocessed dataset feeds into ACDF’s two modules.

Usage	Dataset	Type	Spatiotemporal resolution	Tensor
Correction module – Training input	Pangu-Weather forecast	AI-based global forecast	1 h, 12.5 km	$\mathbf{X}_{\text{pangu}}^t \in \mathbb{R}^{(H+\tau) \times N \times 2}$
	HRCLDAS analysis (history period)	Gridded observation	1 h, 12.5 km	$\mathbf{X}_{\text{LR-obs}}^t \in \mathbb{R}^{H \times N \times 2}$
Correction module – Training label	HRCLDAS analysis (forecast period)	Gridded observation	1 h, 12.5 km	$\mathbf{Y}_{\text{LR-obs}}^t \in \mathbb{R}^{\tau \times N \times 2}$
	Weather stations	In situ observations	1 h, point scale	$\mathbf{Y}_{\text{ST-obs}}^t \in \mathbb{R}^{\tau \times S \times 2}$
Downscaling module – Pretraining input	WRF-d01 simulation	NWP simulation	1 h, 12.5 km	$\mathbf{X}_{\text{d01}}^{i,t} \in \mathbb{R}^{5 \times 5 \times 2}$
	ASTER DEM & land cover	Static geospatial data	500 m	$\mathbf{X}_{\text{terrain}}^i \in \mathbb{R}^{101 \times 101 \times 2}$
Downscaling module – Pretraining label	WRF-d03 simulation	NWP simulation	1 h, 500 m	$\mathbf{Y}_{\text{d03}}^{i,t} \in \mathbb{R}^{101 \times 101 \times 2}$

a τ -hour forecast horizon. Inputs include Pangu-Weather forecast ($\mathbf{X}_{\text{pangu}} \in \mathbb{R}^{(H+\tau) \times N \times 2}$) for the full $(H + \tau)$ -hour sequence and HRCLDAS gridded analyses ($\mathbf{X}_{\text{LR-obs}} \in \mathbb{R}^{H \times N \times 2}$) for the H -hour historical segment. Supervised labels are provided by HRCLDAS fields ($\mathbf{Y}_{\text{LR-obs}} \in \mathbb{R}^{\tau \times N \times 2}$) and point-scale station observations ($\mathbf{Y}_{\text{ST-obs}} \in \mathbb{R}^{\tau \times S \times 2}$) over the τ -hour forecast period. This setup produces 570 spatiotemporal samples, as summarized in Table 4.

Together, these preprocessing steps yield two complementary training sets: (i) dense, terrain-resolved coarse–fine patches for the downscaling module, and (ii) temporally coherent forecast–observation sequences for the correction module. By aligning heterogeneous datasets with the learning objectives of each stage, the pipeline operationalizes ACDF’s decoupled design and establishes a structured foundation for model training. Section 4 builds directly on this foundation to describe implementation and optimization.

4 Model Architecture and Development

Building on the formulation in Section 2 and the datasets in Section 3, this section details how ACDF is operationalized into a working two-stage system. Rather than treating forecast correction and terrain-aware refinement as a single task, ACDF separates them into complementary modules: one that assimilates observations to reduce storm-scale biases, and another that reconstructs fine-scale, terrain-driven variability. This design not only sharpens model interpretability but also ensures forecasts that are both dynamically consistent and operationally actionable. By modularizing these functions, each stage can be independently validated—storm-scale corrections against coarse analyses and terrain refinements against high-resolution labels.

4.1 Terrain-aware downscaling module

The downscaling module functions as a spatial super-resolution network, designed to transform a coarse-resolution (12.5 km) wind field into a physically plausible, high-resolution (500 m) forecast that explicitly accounts for topographical effects ($\mathbf{X}_{\text{terrain}}$). This step is critical because infrastructure exposure is highly sensitive to localized accelerations and sheltering effects that are invisible at coarse resolution.

The module is built on a hierarchical encoder-decoder architecture, structurally similar to a U-Net, but it substitutes standard convolutional layers with more powerful Locally-enhanced Window (LeWin) Transformer blocks (Liu et al., 2021; Wang et al., 2022). As detailed in Figures 5c and 5f, this architecture partitions the feature map into non-overlapping windows and computes self-attention exclusively within these local regions, drastically improving computational efficiency while effectively modeling complex spatial dependencies. To better capture fine-grained local patterns, a depth-wise convolutional block is integrated within the feed-forward network (FFN) of each transformer block.

The workflow proceeds as follows (Figure 5c):

- **Input projection** – The coarse wind field $\mathbf{X}_{\text{d01}}^{i,t} \in \mathbb{R}^{5 \times 5 \times 2}$ is bilinearly interpolated to match the high-resolution terrain grid (500 m, $\mathbb{R}^{101 \times 101 \times 2}$) and concatenated with static terrain features $\mathbf{X}_{\text{terrain}}^i \in \mathbb{R}^{101 \times 101 \times 2}$. Both inputs are projected into a shared high-dimensional space.
- **Encoder** – Stacks of DS blocks progressively reduce spatial resolution while increasing channel depth, extracting multi-scale representations.
- **Decoder** – Symmetrical upsampling stages restore spatial resolution, with skip connections from the encoder to preserve high-frequency spatial details critical for terrain effects.
- **Output projection** – A final deconvolution and

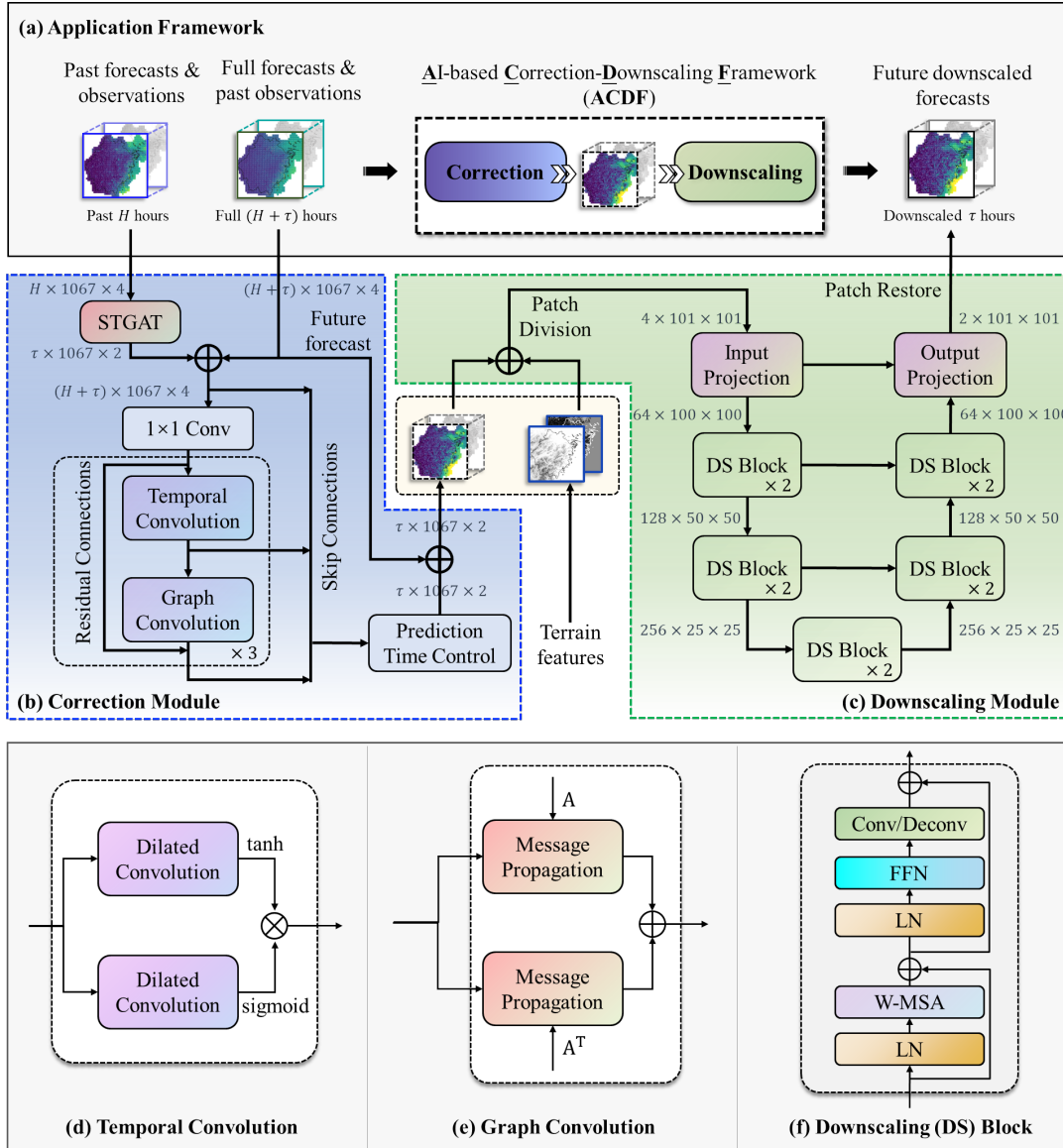


Fig. 5. (a) An overview of the ACDF application framework; The neural network architecture implemented in ACDF consists of (b) correction module and (c) downscaling module. (d) Temporal convolution block and (e) graph convolution block of the correction module. (f) The downscaling (DS) block in the downscaling module, consisting of normalization layer (LN), non-overlapping Window-based Multi-head Self-Attention (W-MSA), Feed-Forward Network (FFN) and convolution or deconvolution (Conv/Deconv) layer.

fully connected layer project the features back to a 2-channel (U, V) wind field $\hat{\mathbf{Y}}_{d03}^{i,t} \in \mathbb{R}^{101 \times 101 \times 2}$.

This hierarchical design ensures that storm-scale circulation patterns are preserved while local terrain effects are superimposed, maintaining both physical plausibility and geographic realism. The module is pre-trained using a mean squared error (MSE) loss against the WRF-simulated reference field:

$$\mathcal{L}_{ds} = \frac{1}{\tau n H' W'} \sum_{i=1}^n \sum_{t=1}^{\tau} \|\hat{\mathbf{Y}}_{ds}^{i,t} - \mathbf{Y}_{d03}^{i,t}\|^2 \quad (4)$$

where τ is the forecast horizon, H' and W' are the dimensions of the high-resolution grid, and i is the patch

index of the total n patches.

4.2 Spatiotemporal correction module

The correction module addresses the bias-correction problem described in Section 2.3, targeting systematic forecast errors in coarse-scale AIWP wind fields. It operates on an $(H + \tau)$ -hour window comprising H hours of historical observations and forecasts, followed by τ hours of future forecasts. This design allows recent observational history to directly anchor bias corrections, ensuring the corrected forecasts remain dynamically consistent with the evolving storm environment.

The temporal-spatial relationship models as follows:

1. **Spatiotemporal Graph Attention Network (STGAT)** – Models spatially heterogeneous and

temporally evolving forecast errors. Using the H -hour historical segment, the STGAT preliminary estimates error patterns and extrapolates them to the forecast horizon, producing a bias field for the full $(H + \tau)$ -hour sequence.

2. **Temporal Convolution (TC) block** – Uses gated dilated inception layers (Figure 5d) to capture temporal patterns. The inception structure applies multiple 1D convolutional filters of different kernel sizes in parallel, enabling the model to discover temporal patterns over various time scales simultaneously. Dilation exponentially increases the receptive field with network depth, allowing the model to efficiently process long input sequences and capture long-term dependencies without a sharp increase in computational cost.
3. **Graph Convolution (GC) block** – Propagates information across the grid according to the learned adjacency matrix (Figure 5e). It employs a mix-hop propagation mechanism, which fuses information from a node’s neighborhood to model spatial dependencies (Wu et al., 2020). This design effectively handles the flow of information between grid points while mitigating the over-smoothing problem common in deep GNNs, thereby preserving important local variations.

These TC and GC blocks are interleaved and stacked, producing a τ -hour correction sequence $\Delta\mathbf{X}_{corr}$. This correction is applied via a residual connection to generate the bias-corrected coarse field: $\hat{\mathbf{X}}_{corr} = \mathbf{X}_{pangu} + \Delta\mathbf{X}_{corr}$. Together, these components allow the model to capture error patterns that evolve across both time and space — a necessity for reducing intensity biases in AIWP forecasts.

4.3 Joint end-to-end optimization

Training follows a sequential, dependency-aware strategy:

1. Pre-train \mathcal{F}_2 (downscaling module) using the WRF dataset and Equation 4. Once stable, its parameters θ_2 are frozen.
2. Train \mathcal{F}_1 (correction module) with the frozen downscaling module appended, ensuring bias correction is optimized for its impact on the final high-resolution forecast.

The joint optimization is governed by a dual-objective loss:

$$\mathcal{L}_{total} = \mathcal{L}_{grid} + \alpha\mathcal{L}_{station} \quad (5)$$

$$\mathcal{L}_{grid} = \frac{1}{\tau N} \sum_{t=1}^{\tau} \|\hat{\mathbf{X}}_{corr}^t - \mathbf{Y}_{LR-obs}^t\|^2 \quad (6)$$

$$\mathcal{L}_{station} = \frac{1}{\tau S} \sum_{t=1}^{\tau} \|\hat{\mathbf{Y}}_{ds}^t - \mathbf{Y}_{ST-obs}^t\|^2 \quad (7)$$

where \mathcal{L}_{grid} enforces meteorological fidelity at the coarse grid scale, and $\mathcal{L}_{station}$ enforces point-level accuracy at weather stations—directly relevant for infrastructure risk. The balance parameter α was tuned empirically and set to 0.01 in this study. In combination, these two objectives balance large-scale meteorological fidelity with local, infrastructure-relevant accuracy, ensuring the final forecasts are both scientifically credible and operationally useful.

4.4 Implementation details

For the correction task, the historical input window was set to $H = 6$ hours and the forecast horizon to $\tau = 12$ hours, balancing timely correction with operational usability. The correction module uses three interleaved TC and GC layers with a dropout rate of 0.3.

The framework was implemented in PyTorch and trained on a NVIDIA GeForce RTX 4090 GPU. Training proceeded in two phases: 1) Downscaling pre-training: 200 epochs, Adam optimizer, batch size 32, learning rate 2×10^{-4} with a step decay; 2) Correction training: 400 epochs, Adam optimizer, batch size 12, learning rate 2×10^{-3} , early stopping with patience of 20 epochs. This staged training strategy operationalizes the decoupled design of ACDF, ensuring both storm-scale corrections and terrain-driven refinements are optimized before evaluation under real-world TC events. This staged strategy directly operationalizes the decoupled ACDF design introduced in Section 2, translating architectural choices into a training workflow that aligns with both physical reasoning and practical deployment.

5 Model Performance Evaluation

The effectiveness of ACDF is evaluated through rigorous out-of-sample tests designed to stress its ability to generalize across diverse TC conditions. Independent test cases are drawn from five severe events withheld under the leave-one-storm-out (LOSO) protocol, ensuring that performance is always measured on storms unseen during training.

The evaluation spans five dimensions central to infrastructure-scale wind forecasting: (i) event-level accuracy and generalizability, assessed through LOSO testing; (ii) temporal stability, testing whether forecast quality is preserved over a 12-hour horizon; (iii) terrain sensitivity, quantifying the added value of the downscaling module in complex landscapes; (iv) robustness under station-only assimilation, evaluating model performance when HRCLDAS input is replaced by interpolated station data; (v) and computational efficiency, reflecting feasibility of real-

time operations.

A central component of the analysis is an ablation test, comparing the full ACDF with a correction-only variant (ACDF-Corr.) to isolate the contribution of the terrain-aware downscaling module. We also include ACDF-S, which assimilates only station-interpolated data instead of HRCLDAS, to test robustness when dense gridded analyses are unavailable. Comparisons with raw Pangu-Weather forecasts and HRCLDAS analyses further benchmark ACDF against both operational forecasts and observation-based references.

For consistency across baselines, two standard metrics are employed:

- Mean Error (ME): Quantifies systematic bias (positive = overestimation; negative = underestimation for wind speed).
- Mean Absolute Error (MAE): Captures the magnitude of deviations from station observations and serves as the principal measure of accuracy.

Where relevant, mean \pm standard deviation values for MAE and ME are reported, calculated across stations and multiple forecast initialization times.

5.1 Aggregate event-level accuracy and generalizability

Table 5 reports station-scale prediction errors for five independent TC events under the LOSO protocol. ACDF attains the best overall accuracy, with an average MAE of 1.374 m/s, improving upon the baseline Pangu forecast (2.245 m/s) by 38.8%. It also matches/slightly surpasses the mesoscale reference HRCLDAS (1.404 m/s on average), indicating that the two-stage correction–downscaling design effectively closes the gap between coarse global guidance (Pangu) and observation-assimilated products (HRCLDAS) while operating at far lower computational cost. Event-wise reductions versus Pangu are consistent—46.6% (Muifa), 41.1% (Lekima), 40.2% (Haikui), 35.1% (Mitag), and 31.2% (Hagupit)—demonstrating robustness across tracks and intensities.

Ablation results clarify each module’s contribution. The correction-only variant (ACDF-Corr.) lowers average MAE to 1.447 m/s (−35.5% vs Pangu), showing that assimilating recent observations efficiently removes storm-scale biases in intensity and structure. Adding the terrain-aware downscaling module (i.e., ACDF) yields the lowest errors (1.374 m/s), capturing ridge speed-up and valley sheltering that are invisible at coarse resolution.

Biases are likewise mitigated. The average ME decreases from 1.584 m/s (Pangu) to −0.421 m/s (ACDF), indicating a more balanced representation across weak- and strong-wind regimes. Wind-direction errors also improve modestly at the aggregate level (from 43.314° to 40.088°, with HRCLDAS

at 39.476°), which is operationally adequate given the known uncertainties in mesoscale directional labels.

Regarding dispersion, the reported standard deviations (STDs) are large across all methods, reflecting strong spatiotemporal heterogeneity in storm impacts and label variability; importantly, ACDF’s MAE dispersion (1.515 m/s) is lower than Pangu’s (1.820 m/s) and slightly better than HRCLDAS (1.605 m/s). Two factors explain this behavior without undermining the central finding: (i) ACDF’s gains over Pangu are substantial and systematic, especially in the high-wind regime that drives fragility; and (ii) the mesoscale target (HRCLDAS) itself exhibits sizable STDs, so ACDF’s near-parity with HRCLDAS suggests that much of the remaining dispersion is label-side rather than model-induced. Overall, ACDF delivers lower mean error, reduced bias, and tighter spread than the raw AI forecast, providing stable and asset-relevant guidance for downstream risk assessment.

Figure 6 further illustrates the distributional benefits of ACDF. In the high-wind regime (>20 m/s)—critical for transmission tower vulnerability—Pangu consistently underestimates observed winds, while ACDF significantly narrows this gap. The alignment with observed distributions, particularly in the upper tail where fragility functions steeply increase failure probability, demonstrates ACDF’s operational value. Taking a representative fragility curve as shown in Figure 6f, the probability of tower failure rises steeply once wind speeds exceed 20 m/s, reaching 0.5 at around 25 m/s. When these fragility thresholds are overlaid on the probability distributions of each TC (Figures 6(a–e)), it is clear that Pangu rarely captures the density of extreme winds, while ACDF produces distributions that closely match observations.

The advantage of ACDF becomes even more evident in the gray-shaded region corresponding to total tower failure (100% probability). Here, Pangu’s forecasts rarely reach the critical thresholds, while ACDF succeeds in reproducing the observed density of extreme winds. This distinction is operationally crucial: because tower failure probability is accumulated over time (details in Section 6.3), repeated underestimation of high winds—even by small margins—can lead to severe misjudgments in system-level risk. By more faithfully capturing these upper-tail extremes, ACDF ensures that forecasts translate into more reliable and realistic failure probability assessments.

Taken together, these results demonstrate that ACDF not only corrects TC-scale biases and lowers mean error but also captures the high-wind extremes most relevant for infrastructure risk, offering clear advantages over the Pangu baseline.

5.2 Temporal correction stability

Beyond event-level accuracy, the temporal stability of forecasts is equally critical for operational reliability.

Table 5. Station-scale mean \pm standard deviation of MAE and ME for five LOSO test storms (Best mean values in **bold**; second-best in underline (for ME, closeness to zero is considered “better”))

Testing Event (ID)	Model	MAE _{spd} (m/s)	ME _{spd} (m/s)	MAE _{dir} (°)
Haikui (1211)	Pangu	2.374 \pm 1.890	1.821 \pm 2.427	38.668 \pm 40.559
	ACDF-Corr.	1.600 \pm 1.696	-0.073\pm2.330	<u>37.341\pm40.528</u>
	ACDF-S	<u>1.570\pm1.653</u>	-0.307 \pm 2.259	38.305 \pm 41.684
	ACDF (Ours)	1.419\pm1.506	<u>-0.168\pm2.062</u>	36.008\pm39.857
	HRCLDAS (Target)	1.705 \pm 1.783	0.190 \pm 2.459	39.282 \pm 42.441
Lekima (1909)	Pangu	2.705 \pm 2.052	1.948 \pm 2.780	42.266 \pm 43.585
	ACDF-Corr.	1.631 \pm 1.813	-0.505 \pm 2.386	<u>39.906\pm42.535</u>
	ACDF-S	1.590\pm1.725	-0.638 \pm 2.258	41.606 \pm 43.352
	ACDF (Ours)	<u>1.594\pm1.760</u>	-0.385\pm2.343	39.529\pm42.434
	HRCLDAS (Target)	1.600 \pm 1.811	-0.230 \pm 2.406	39.154 \pm 42.074
Mitag (1918)	Pangu	2.001 \pm 1.697	1.315 \pm 2.270	47.194 \pm 44.504
	ACDF-Corr.	1.329 \pm 1.501	<u>0.582\pm1.919</u>	<u>43.747\pm43.661</u>
	ACDF-S	1.290\pm1.437	-0.633 \pm 1.825	48.074 \pm 45.680
	ACDF (Ours)	<u>1.299\pm1.452</u>	-0.488\pm1.886	43.403\pm43.484
	HRCLDAS (Target)	1.252 \pm 1.502	-0.189 \pm 1.946	40.321 \pm 41.913
Hagupit (2004)	Pangu	1.792 \pm 1.604	1.128 \pm 2.124	43.866 \pm 42.581
	ACDF-Corr.	1.296 \pm 1.418	-0.718 \pm 1.782	<u>42.257\pm42.528</u>
	ACDF-S	<u>1.273\pm1.374</u>	-0.696 \pm 1.739	49.249 \pm 46.981
	ACDF (Ours)	1.233\pm1.343	-0.585\pm1.727	40.810\pm41.949
	HRCLDAS (Target)	1.166 \pm 1.328	-0.429 \pm 1.715	38.822 \pm 40.656
Muifa (2212)	Pangu	2.452 \pm 1.597	1.827 \pm 2.287	45.873 \pm 43.613
	ACDF-Corr.	1.360 \pm 1.510	-0.604 \pm 1.940	<u>42.450\pm43.103</u>
	ACDF-S	<u>1.341\pm1.447</u>	-0.713 \pm 1.839	44.753 \pm 44.457
	ACDF (Ours)	1.309\pm1.431	-0.456\pm1.885	41.448\pm42.480
	HRCLDAS (Target)	1.287 \pm 1.456	-0.394 \pm 1.903	40.325 \pm 42.812
Average	Pangu	2.245 \pm 1.820	1.584 \pm 2.418	43.314 \pm 43.087
	ACDF-Corr.	1.447 \pm 1.604	-0.501 \pm 2.102	<u>40.994\pm42.483</u>
	ACDF-S	<u>1.416\pm1.544</u>	-0.597 \pm 2.008	44.354 \pm 44.684
	ACDF (Ours)	1.374\pm1.515	-0.421\pm2.002	40.088\pm42.080
	HRCLDAS (Target)	1.404 \pm 1.605	-0.212 \pm 2.121	39.476 \pm 41.899

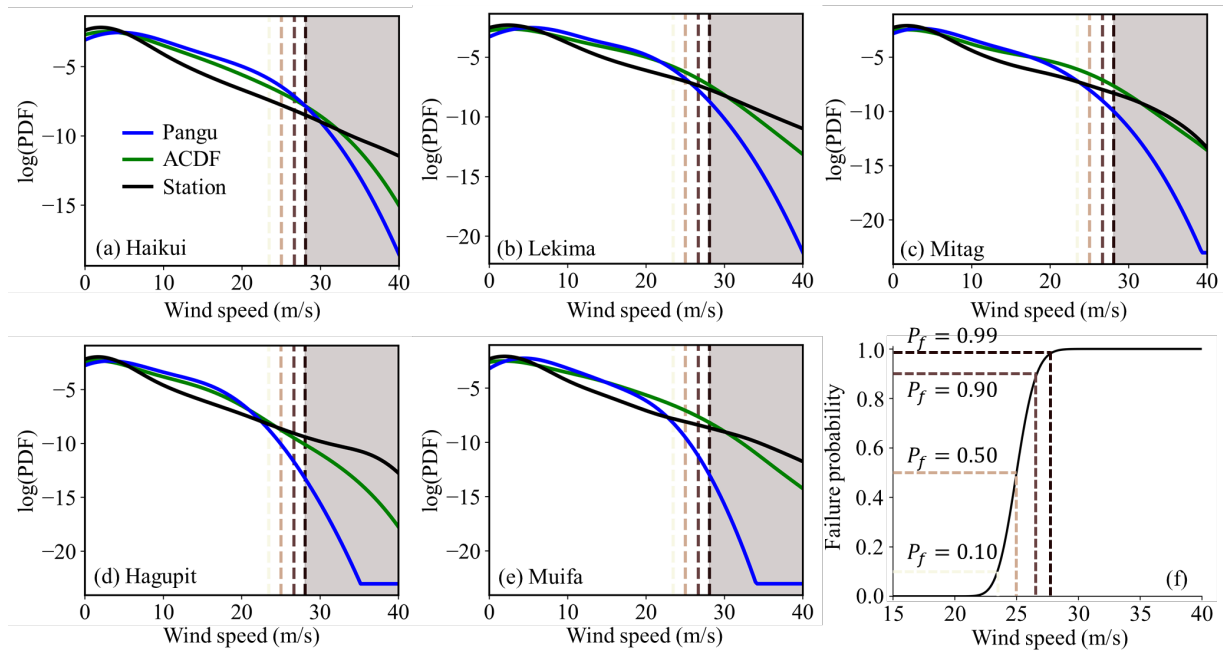


Fig. 6. (a-e) Probability density functions for all station samples across five severe TC events, showing that ACDF aligns closer with observations and reduces the high-wind underestimation seen in Pangu forecasts; and (f) a typical fragility function for the transmission towers.

Forecasts that fluctuate sharply over time can undermine user confidence and complicate decision-making, even if their average accuracy appears acceptable. To evaluate this aspect, we focus on an 18-hour analysis window spanning from 6 hours before landfall to 12 hours after, which captures the most hazardous stage of the event when wind speeds typically exceed 15 m/s and forecast errors have the greatest impact. Within this window, multiple forecast cycles are considered, each providing a 12-hour forecast horizon. This setup allows us to assess not only pointwise performance but also the consistency of forecast quality over successive updates as the storm evolves.

As shown in Figure 7a, both Pangu and ACDF maintain relatively steady MAE values across the 12-hour forecast horizon. However, their absolute accuracy diverges. Pangu’s errors remain consistently above 3 m/s, whereas ACDF sustains values below 2 m/s throughout. Pangu also shows an anomalous trend of decreasing error with lead time. This trend aligns with post-landfall weakening in the storms’ intensity time series and reflects tropical cyclone evolution rather than genuine forecast skill: early timesteps coincide with peak intensity when biases are greatest, while later timesteps fall into the decay phase when weaker winds naturally reduce error magnitudes.

The differences become more pronounced when focusing on high-wind conditions (Figure 7b). Here, Pangu’s performance is not only less accurate but also highly

unstable, with pronounced oscillations in mean error and a much broader spread across forecast cycles. In contrast, ACDF delivers a substantially narrower error distribution and smoother temporal evolution, consistently maintaining mean MAE values below 4 m/s. The interquartile ranges (IQRs) plotted in Figure 7 further support this finding: ACDF exhibits tighter IQRs than Pangu across all lead times, indicating reduced variability and greater robustness from one forecast cycle to the next.

5.3 Terrain sensitivity

The terrain-stratified analysis uses the same 18-hour window as in Section 5.2—from 6 h before landfall to 12 h after—so that temporal and spatial variations are examined under identical storm stages. Figures 8(a-e) presents the regression results between pre-trained downscaling model predictions and WRF-simulated 500 m reference winds for the five independent TC cases. Across Haikui, Lekima, Mitag, Hagupit, and Muifa, the coefficient of determination (R^2) reaches 0.93, 0.95, 0.86, 0.95, and 0.91, respectively. These consistently high correlations demonstrate that the terrain-aware downscaling module reconstructs fine-scale wind structures with remarkable fidelity and generalizes well across storms of differing tracks and intensities. The strong cross-event agreement confirms that ACDF does not simply memorize terrain patterns from training storms but robustly captures the physical relationship between large-scale flow and local topographic modulation.

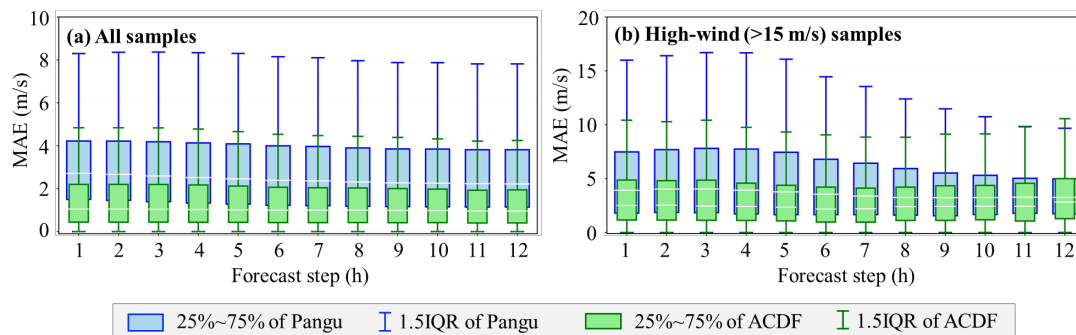


Fig. 7. Temporal evolution of wind speed MAE for (a) all samples and (b) high-wind samples over a 12-hour forecast horizon.

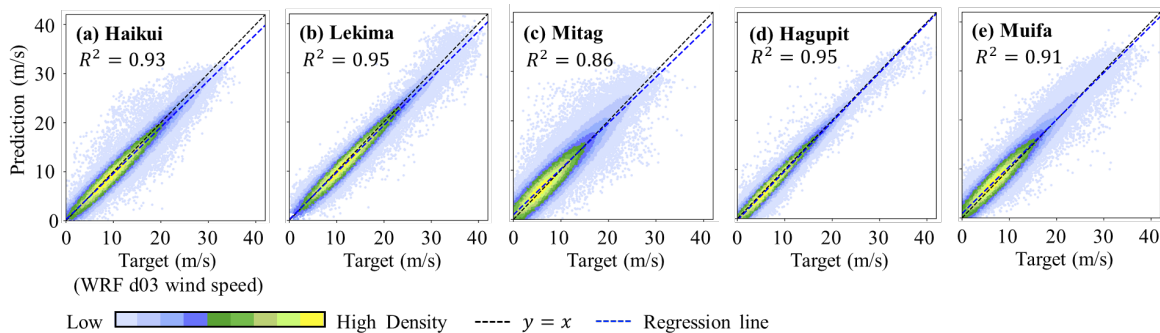


Fig. 8. LOSO tests of downscaling predicted versus WRF wind speeds for the (a) Haikui, (b) Lekima, (c) Mitag, (d) Hagupit, and (e) Muifa events.

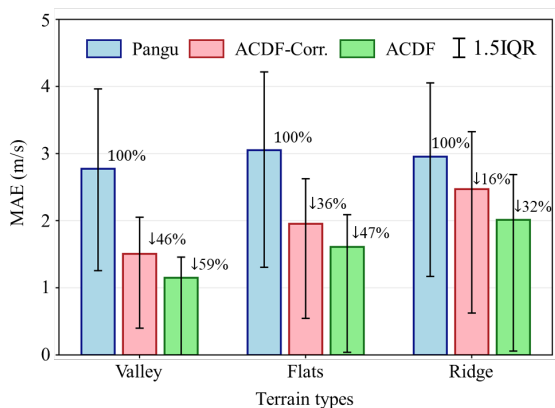


Fig. 9. Wind-speed MAE stratified by terrain types: valleys ($TPI < -50$ m), flats ($-50 \text{ m} \leq TPI \leq 50$ m), and ridges ($TPI > 50$ m).

Using the Topographic Position Index (TPI) (Weiss, 2001), sites are categorized as valleys (< -50 m), flats ($-50 \text{ m} \leq TPI \leq 50$ m), and ridges (> 50 m) to quantify terrain-specific performance (Figure 9). Pangu’s errors show little differentiation among terrain classes, whereas ACDF progressively refines predictions: bias correction (ACDF-Corr.) reduces MAE by 46%, 36%, and 16% for valleys, flats, and ridges, and adding the downscaling module further cuts errors by 59%, 47%, and 32%, respectively. Although relative gains are smaller on ridges, they are especially valuable because these zones host the highest winds and most vulnerable assets. Moreover, ACDF markedly narrows the IQR of MAE across all classes, indicating reduced dispersion and greater forecast reliability. Altogether, the framework achieves terrain-consistent, temporally stable, and cross-event-generalizable performance—transforming coarse AI forecasts physically credible, infrastructure-relevant wind fields.

5.4 Robustness under station-only data assimilation (ACDF-S)

Having established ACDF’s skill with multi-source assimilation, we next stress-test its robustness in data-sparse conditions. To test robustness in data-sparse settings, we replace HRCLDAS inputs with station-interpolated fields while keeping the architecture unchanged. As presented in Table 5, across LOSO events, ACDF-S achieves an average MAE of 1.416 m/s—a 36.9% reduction vs Pangu and within 0.042 m/s of the full ACDF (1.374 m/s). Bias control is similar (ME -0.597 m/s for ACDF-S vs -0.421 m/s for ACDF). Directional errors are larger for ACDF-S (44.354°), reflecting the loss of dense gridded constraints, but wind-speed skill—the primary driver of fragility—remains strong. The small performance gap confirms practical implementation capacity across heterogeneous data regimes.

That is in practice, ACDF can operate in two modes: a baseline, station-only mode (ACDF-S) for sparse regions

and a multi-source mode (ACDF) when gridded analyses are available. Thus, operational agencies can tailor assimilation strategies to available resources—leveraging simple setups where data are sparse, and maximizing accuracy when dense products exist.

5.5 Computational efficiency

A defining advantage of the ACDF is its computational efficiency, which makes real-time operational deployment feasible. For a single forecast cycle covering a 12-hour lead time, the complete correction and downscaling process requires only approximately 25 seconds of inference time on an NVIDIA 4090 GPU, with the downscaling module accounting for 95% of this cost. By contrast, generating a comparable high-resolution forecast using the traditional physics-based WRF model would require several hours of runtime. This three-orders-of-magnitude speedup transforms what was once a computationally prohibitive task into one suitable for rapid decision-making during evolving TC events.

These efficiency gains do not come at the expense of accuracy. Across evaluations, ACDF consistently delivers forecasts that are accurate, unbiased, and reliable, while also sustaining skill across diverse terrains and storm conditions. The ability to produce terrain-aware, infrastructure-scale wind fields in seconds rather than hours underscores ACDF’s practical value: it bridges the gap between research-grade models and real-time operational needs, establishing itself as a field-ready framework for infrastructure-scale wind forecasting under TC conditions.

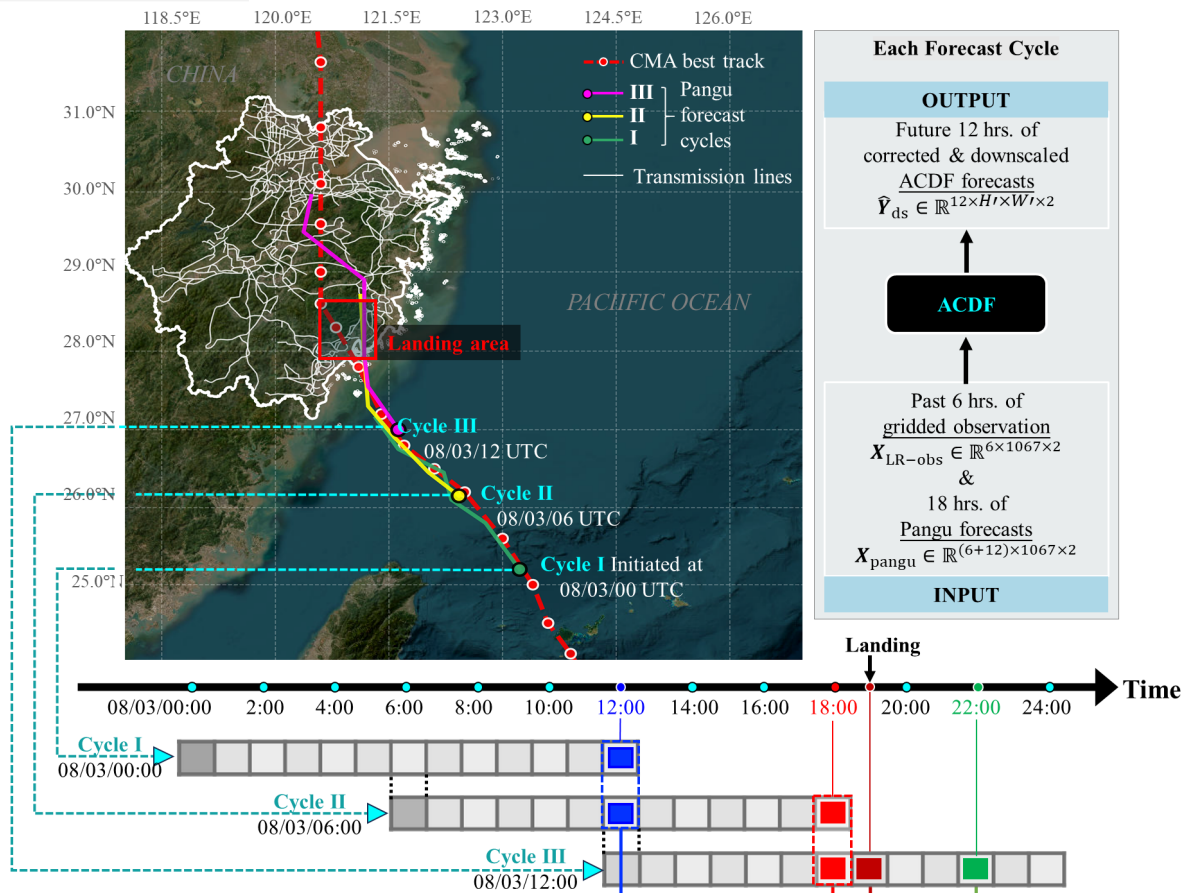
6 Case Study: Enhancing Zhejiang Power Grid Resilience with Sub-kilometer Wind and Risk Forecasts During Typhoon Hagupit

6.1 Event setup and forecast configuration

To illustrate ACDF’s end-to-end operational capacity, we present Severe Typhoon Hagupit (ID: 2004) in Zhejiang Province as a representative use case. The case traces the full workflow—assimilation and bias correction of AIWP mesoscale forecasts, sub-kilometer terrain-aware downscaling, and dynamic tower- and line-level risk estimation—showing how ACDF converts raw AIWP output into infrastructure-specific intelligence fast enough for operations during a rapidly evolving landfalling TC.

As shown in Figure 10a, Pangu-Weather was run in three forecast cycles on 3 August 2020 at 00:00, 06:00, and 12:00 UTC. At each cycle, ACDF (i) ingests the past 6 h and the next 12 h of raw Pangu mesoscale forecasts, (ii) assimilates 6 h of HRCLDAS analyses together with 2,513 ground-station

(a) Forecast cycle setting



(b) Wind field comparison

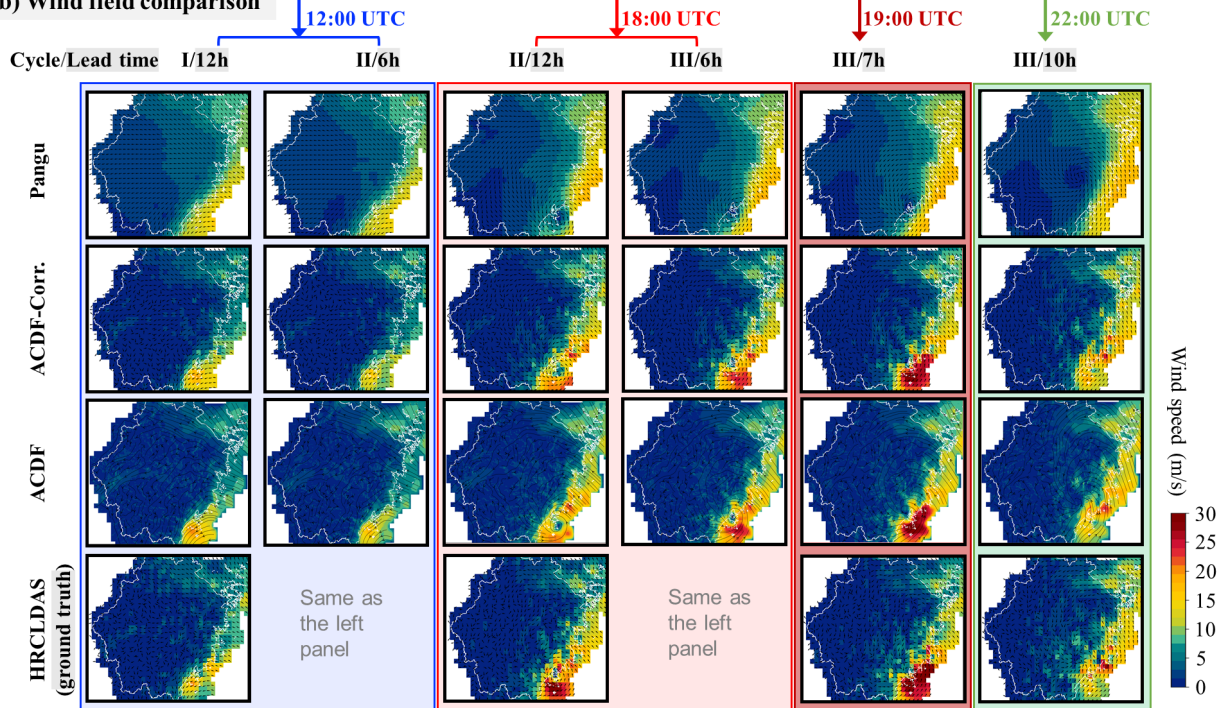


Fig. 10. (a) CMA best track and Pangu forecast tracks for Typhoon Hagupit at three forecast cycles; (b) comparison of Pangu, ACDF-Corr., ACDF and HRCLDAS wind fields at four key times with different lead times.

observations, (iii) performs bias correction at 12.5 km, and (iv) downscales to 500-m resolution. This tightly coupled process produces future 12-hour terrain-resolved, unbiased wind field forecasts in real time and drives risk forecasts for 780 transmission lines, spanning about 9,500 km across $\sim 105,500$ km² of Zhejiang.

The lead hours (shown in Figures 10(a,b)) for the four key analysis times used in Section 6.2 are:

- 12:00 UTC (pre-landfall): 12 h lead from Cycle I and a 6 h lead from Cycle II.
- 18:00 UTC (close to landfall): 12 h lead from Cycle II and a 6 h lead from Cycle III.
- 19:00 UTC (landfall): 7 h lead from Cycle III.
- 22:00 UTC (inland decay): 10 h lead from Cycle III.

These staggered lead times let us assess how ACDF behaves both earlier (12 h) and closer (6–10 h) to impact as new observations arrive—an operationally critical property during rapid TC evolution.

6.2 Wind field enhancement

For each analysis time (12:00, 18:00, 19:00, 22:00 UTC), Figure 10b juxtaposes two forecasts when available—one issued in an earlier cycle (longer lead) and one in a later cycle (shorter lead)—against HRCLDAS. This layout isolates the effect of lead time while holding the valid time fixed.

12:00 UTC (pre-landfall; Cycle I 12 h vs. Cycle II 6 h). ACDF-Corr. reduces Pangu’s storm-scale bias; full ACDF then projects those corrections into a terrain-aware 500 m field, sharpening coastal gradients and ridge–valley contrasts without spurious extremes. The shorter-lead Cycle II forecast best matches HRCLDAS.

18:00 UTC (close to landfall; Cycle II 12 h vs. Cycle III 6 h). The lead–skill contrast strengthens. Pangu underestimates the compact coastal core; ACDF-Corr. improves intensity and placement; ACDF at 6 h lead (Cycle III) aligns most closely with HRCLDAS in both magnitude and footprint.

19:00 UTC (landfall; Cycle III 7 h). With fresh assimilation, ACDF maintains the observed amplitude over the right-hand semicircle of the TC track and captures localized coastal maxima missed by Pangu.

22:00 UTC (inland decay; Cycle III 10 h). ACDF preserves the >10 m/s footprint and terrain-conditioned peaks near 20 m/s, showing the model maintains forecast accuracy across the event lifecycle.

Across timestamps, shorter-lead cycles consistently yield higher skill, especially in the high-wind tail, while longer-

lead forecasts are smoother and left-biased in intensity. This demonstrates the operational value of real-time cycling: each 6-hour update tightens TC-scale bias through assimilation, and ACDF then projects those corrections into sub-kilometer, terrain-aware structure.

Figure 11 steps from province to asset scale to show why bias correction and downscaling are both required for credible line-failure forecasting. In the province scale column (Figures 11(a-c)), the raw Pangu field is smooth and weak, blurring the compact coastal wind core at landfall. ACDF-Corr. corrects storm-scale intensity and placement, and the full ACDF preserves those corrections while adding terrain-conditioned structure at 500-m resolution. In the landfall zone column (Figures 11(d-f)), station dots expose the differences. Pangu concentrates values in the 0–10 m/s range and misses the coastal high-wind corridor. ACDF-Corr. restores mesoscale gradients consistent with the evolving storm, and ACDF resolves ridge speed-up and valley sheltering along the mountainous coastline—features required to explain observed extremes. The payoff appears at the line segments column (Figures 11(g-i)). Pangu and ACDF-Corr. both yield nearly uniform loading along spans; only ACDF produces spatial variability at the tower–span scale—localized maxima on exposed ridges and minima in sheltered valleys—that drives fragility-based failure probabilities. The topography/line overlay (Figure 11k) clarifies the orographic controls, while the tower-level distributions (Figure 11j) confirm that Pangu deviates noticeably from station observation; ACDF matches stations and recovers the >10 m/s tail that governs failure risk. Together, these panels demonstrate compatibility with downstream reliability models: without removing storm-scale bias and restoring sub-kilometer variability, line-level risk over tens to hundreds of kilometers cannot be estimated credibly; with ACDF, it can.

6.3 Infrastructure risk forecasting

The objective is then to translate ACDF’s sub-kilometer winds into actionable, real-time risk for the transmission network. We couple the 500-m wind fields to fragility models for Zhejiang’s $\sim 9,500$ km of 780 transmission lines supported by 32,458 towers, producing tower- and line-level failure probability forecasts with lead times of up to 12 h.

Risk mapping. For each tower j at hour t during the 12-hour forecast period, ACDF supplies 10-m wind speed $v_{j,t}$ and attack angle $\theta_{j,t}$. An angle-dependent lognormal fragility converts $(v_{j,t}, \theta_{j,t})$ to instantaneous tower failure probability $P'_{j,t}$ after marginalizing capacity uncertainty R by Monte Carlo. Temporal cumulative risk uses a survival update—once a tower fails it remains failed—yielding the cumulative probability P_j . Line risk treats each line i as a series system, $P_{i,t}^{Line} = 1 - \prod_{j \in \text{line}_i} (1 - P_{j,t})$. Full formulas (as well documented in Huang & Wang, 2024; Xue et al., 2020) and settings follow standard reliability practice are provided in

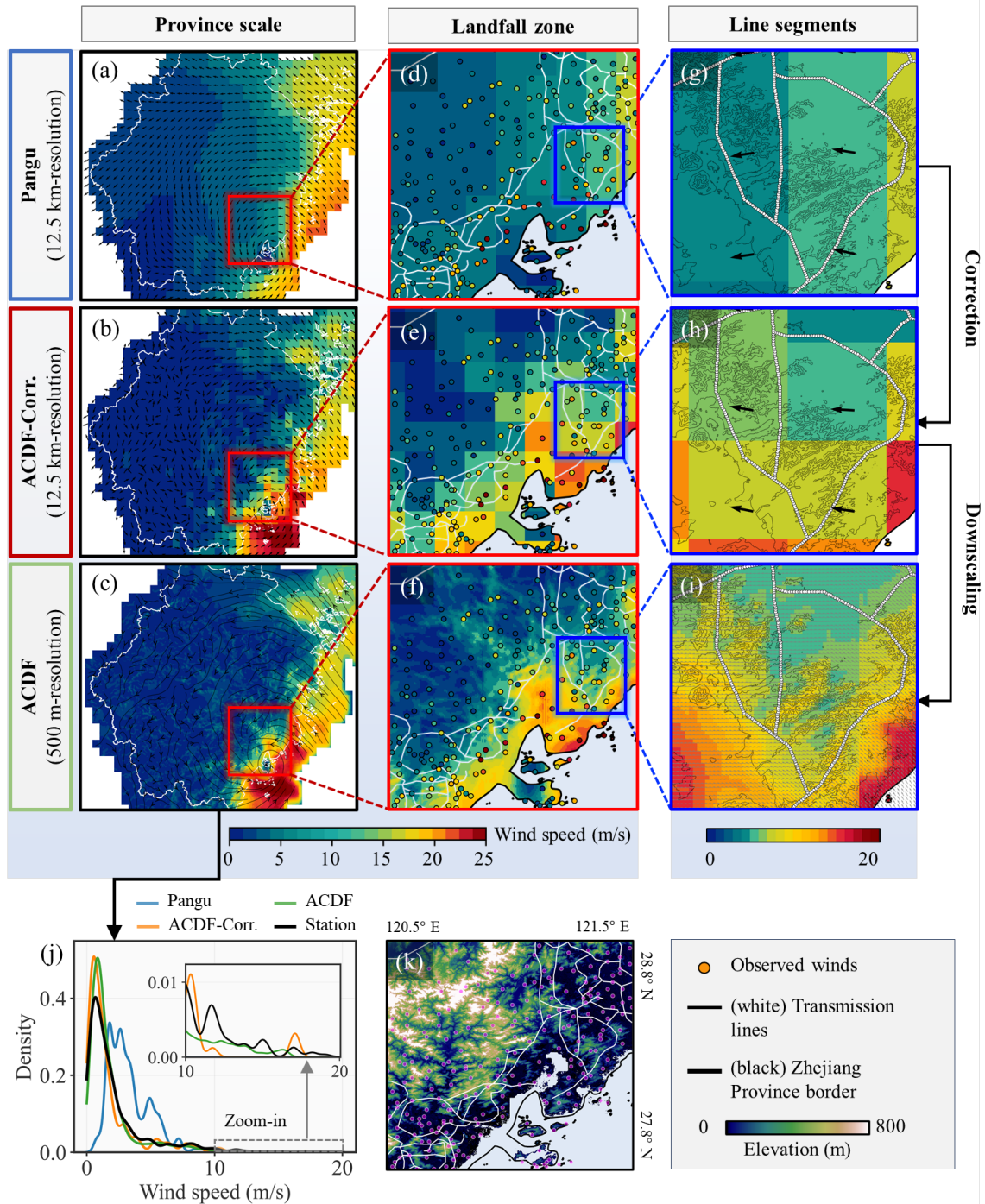


Fig. 11. Multi-scale comparison at 18:00 UTC, 3 Aug 2020 (close to landfall). Columns: Province scale—(a) Pangu (12.5 km), (b) ACDF-Corr. (12.5 km), (c) ACDF (500 m); Landfall zone—(d) Pangu, (e) ACDF-Corr., (f) ACDF with station observations; Line segments—(g) Pangu, (h) ACDF-Corr., (i) ACDF along a transmission corridor; (j) tower-level wind-speed distributions (Pangu, ACDF-Corr., ACDF, station observations); (k) Topography with transmission lines. ACDF retains storm-scale corrections and adds 500 m terrain-modulated structure (ridge speed-up, valley sheltering), recovers the observed >10 m/s tail, and yields asset-scale variability necessary for credible tower/line failure forecasting.

Appendix A (Equations A1–A5; Table A1). For Hagupit we use a single low-capacity tower class and conditional independence; utilities can substitute type-specific fragilities and dependence structures without changing the workflow.

System-level patterns. Figure 12 visualizes line-level

failure probabilities from Cycle III at 18:00 (close to landfall), 19:00 (landfall), and 00:00 UTC (final forecast time). Because Pangu strongly underestimates winds, no lines exceed the operational threshold ($P_i^{Line} = 0.01$) in Figures 12(c–e), highlighting its unsuitability for network-scale risk prediction. In contrast, ACDF (Figures 12(f–h)) delineates a coherent coastal high-risk corridor aligned with the right-

hand semicircle of maximum TC winds and tracks its evolution through the event. Among 780 lines, ACDF elevates only a small subset as potentially critical—precisely the triage operators need. Notably, it flags the actual failed line (ID 73) (Figures 12(i-k); $P_{73}^{line} = 1.00$) and highlights additional corridors (IDs 68, 77, 81) where conductor galloping/over-stress was reported, while Pangu misses all. These are not spurious “false alarms” but physically plausible risk signals. A mild positive bias is operationally acceptable, as it focuses attention on truly hazardous corridors within a large network. The time series in Figure 12i shows line failure probabilities rising and then stabilizing as high-wind exposure accumulates—behavior consistent with the survival update and observed impacts—and illustrates lead-time utility: successive updates converge quickly on a stable, high-confidence set of critical members rather than “everything high-risk” or “nothing at risk.” Notably, for line 73, the recorded actual failure occurred at 18:00 UTC, precisely when the ACDF-predicted failure probability reached 1.00, offering a valuable 5-hour lead time for grid emergency decision-making and demonstrating strong temporal alignment with the actual damage event.

Asset-level differentiation (Figure 13). Over complex landfall terrain, ACDF-Corr. (correction only) yields near-uniform span loads along Line 73 and muted failure probabilities. The full ACDF resolves valley channeling and ridge speed-up, producing localized wind maxima >20 m/s and sharp tower-to-tower contrasts in $P_{j,t}$. Panel Figure 13a overlays final tower probabilities on topography, while Figure 13b co-plots (along the line) final P_j , maximum wind over 13:00–00:00 UTC, and elevation—revealing one-to-one correspondence between orographic exposure, wind peaks, and failure hotspots. This granularity pinpoints which spans/towers warrant pre-emptive switching, targeted inspection, or staged restoration.

Operational cadence. Each AIWP forecast-to-risk cycle completes in ~ 25 s on a single RTX 4090 GPU, providing 12-hour lead time for proactive operations. The same pipeline accommodates AIWP ensemble inputs to generate probabilistic risk products (forecast uncertainty), without architectural changes.

This case study shows a complete path from global forecasts to decisions: ACDF corrects and downscales in seconds and outputs tower- and line-level failure probabilities forecasts with 12-hour lead time, localizing risk hot spots before landfall at the resolution of individual assets, creating concrete opportunities for targeted inspections, pre-emptive switching, and staged restoration. The same workflow generalizes across storms, grids, and data regimes, positioning ACDF as an immediately useful tool for resilience operations.

7 Conclusion

This work addresses an implementation gap in climate resilience: turning fast, global AI weather prediction into asset-scale, impact-based intelligence that operators can use. We introduced the AI-based Correction–Downscaling Framework (ACDF), a modular pipeline that first removes storm-scale biases from AI weather forecasts and then restores sub-kilometer, terrain-conditioned wind structure, yielding a 500-m, province-scale wind product expressly designed for infrastructure risk forecasting.

Across 11 historical typhoons, ACDF reduced station-scale wind-speed MAE by 38.8% relative to Pangu-Weather, matched the accuracy of observation-assimilated mesoscale analyses, and delivered a ~ 25 times increase in spatial resolution—while running in ~ 25 s per 12-h cycle on a single GPU. Ablations confirmed complementary roles: correction fixes intensity and placement errors; downscaling supplies the terrain detail that governs structural loading. ACDF maintained temporal stability across the 12-h horizon, generalized across storms and terrain, and remained effective in a station-only mode (ACDF-S), preserving $\sim 95\%$ of headline gains when gridded analyses were unavailable.

The Typhoon Hagupit (2020) case study demonstrated end-to-end operational value. ACDF reproduced observed high-wind tails, revealed a coherent coastal risk corridor, and flagged the transmission line that later failed, enabling tower- and line-level failure probabilities that aligned with observed impacts. Six-hour cycling provided a clear lead-time/skill trade-off: as new observations arrived, storm-scale bias tightened and those corrections were projected into sub-km structure—precisely the regime that drives asset fragility.

Limitations and priorities for future work remain. Our experiments are region-specific; broader trials are needed to assess transferability across coastal settings and network types. The current workflow is driven by deterministic AI forecasts; propagating meteorological uncertainty through to failure probabilities via ensemble drivers is a natural next step. Fragility modeling used a single conservative tower class and assumed conditional independence; adopting type-specific fragilities and spatial/temporal dependence models would sharpen risk estimates. Beyond wind-driven outages, ACDF’s modular design is readily extensible to multi-hazard contexts (e.g., rainfall-induced failures) and to other networks (transportation, water, communications).

Despite these caveats, ACDF offers a practical pathway to operational, impact-based early warning. It is fast, interpretable, and scalable; it couples naturally with ensemble AI drivers, outage propagation models, and restoration planning. By bridging global AI forecasts to actionable, asset-level risk, ACDF advances how civil infrastructure prepares for and rides through tropical cyclones—supporting

decisions that safeguard lives and reduce economic losses under a changing climate.

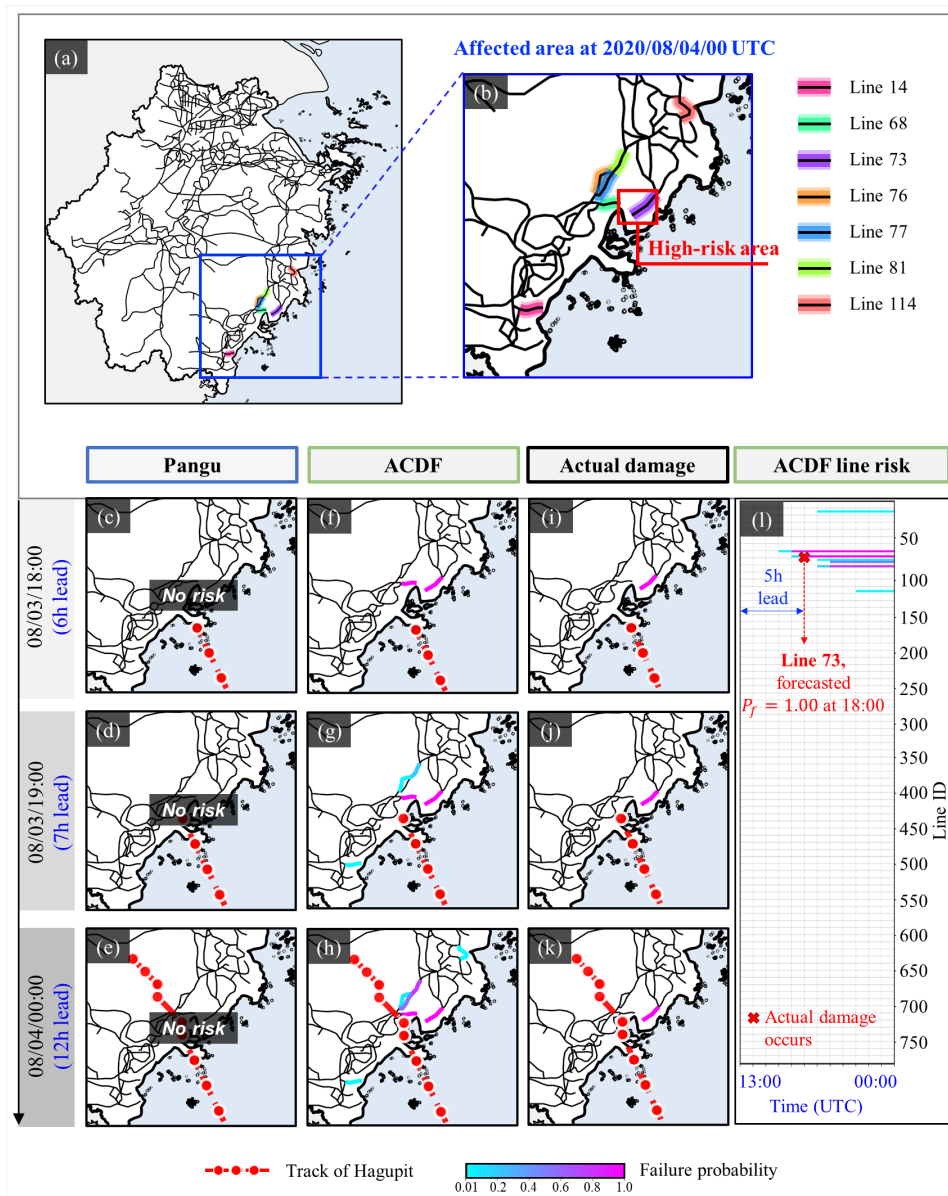


Fig. 12. Comparative risk assessment for the Zhejiang transmission system during Typhoon Hagupit. (a) Province-wide map of line-level failure probabilities and (b) zoom near the landfall zone. (c–k) Line failure probabilities at three key valid times—18:00 (close to landfall), 19:00 (landfall), and 00:00 UTC (final forecast time)—comparing (c, d, e) Pangu and (f, g, h) ACDF against (i, j, k) recorded line failures; and (l) Time-varying failure probabilities across all lines.

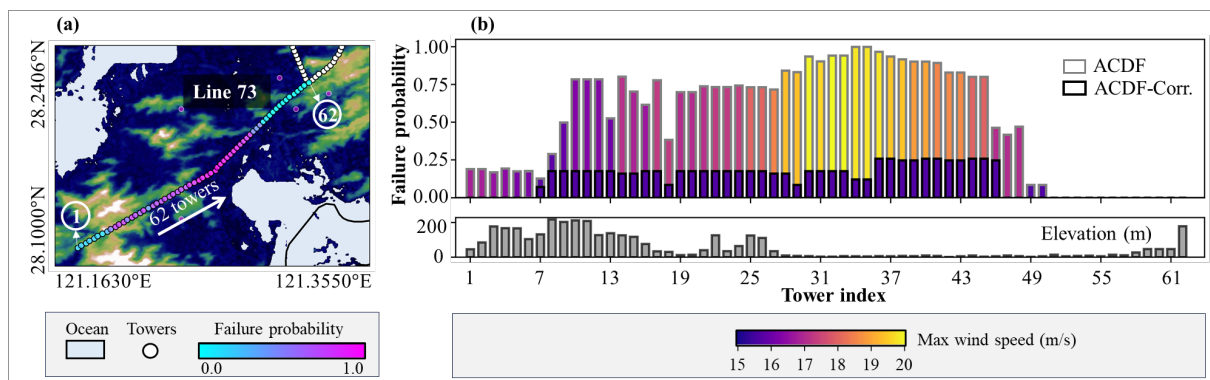


Fig. 13. (a) Surrounding topography and final failure probabilities of the Line 73; (b) Final failure probabilities, maximum wind speeds from 13:00 UTC August 3rd to 00:00 UTC August 4th and elevations of towers in Line 73.

Acknowledgment

This research was co-supported by Zhejiang Department of Science & Technology (Grant No. 2024C03255) and by the State Grid Zhejiang Electric Power Co., Ltd. (Grant No. 5211DS25000L).

References

- Abrams, M., Crippen, R., & Fujisada, H. (2020). ASTER Global Digital Elevation Model (GDEM) and ASTER Global Water Body Dataset (ASTWBD). *Remote Sensing*, 12(7), 1156. <https://doi.org/10.3390/rs12071156>
- Allen, A., Markou, S., Tebbutt, W., Requeima, J., Bruinsma, W.P., Andersson, T.R., Herzog, M., Lane, N.D., Chantry, M., Hosking, J.S., & Turner, R.E. (2025). End-to-end data-driven weather prediction. *Nature*. <https://doi.org/10.1038/s41586-025-08897-0>
- ASCE. (2015). Design of Lattice Steel Transmission Structures. <https://doi.org/10.1061/9780784413760>
- Bauer, P., Thorpe, A., & Brunet, G. (2015). The quiet revolution of numerical weather prediction. *Nature*, 525(7567), 47–55. <https://doi.org/10.1038/nature14956>
- Bi, K., Xie, L., Zhang, H., Chen, X., Gu, X., & Tian, Q. (2023). Accurate medium-range global weather forecasting with 3D neural networks. *Nature*, 619(7970), 533–538. <https://doi.org/10.1038/s41586-023-06185-3>
- Chen, L., Zhong, X., Zhang, F., Cheng, Y., Xu, Y., Qi, Y., & Li, H. (2023). FuXi: a cascade machine learning forecasting system for 15-day global weather forecast. *npj Climate and Atmospheric Science*, 6(1), 190. <https://doi.org/10.1038/s41612-023-00512-1>
- China Power. (2019). Retrieved from <http://www.chinapower.com.cn/dwshzr/20190819/1283961.html>
- Coughlan De Perez, E., Van Den Hurk, B., Van Aalst, M.K., Amuron, I., Bamanya, D., Hauser, T., Jongma, B., Lopez, A., Mason, S., Mender De Suarez, J., Pappenberger, F., Rueth, A., Stephens, E., Suarez, P., Wagemaker, J., & Zsoter, E. (2016). Action-based flood forecasting for triggering humanitarian action. *Hydrology and Earth System Sciences*, 20(9), 3549–3560. <https://doi.org/10.5194/hess-20-3549-2016>
- Cui, Y., Feng, K., Ma, W., & He, B. (2025). Reinforcement learning for optimizing hurricane evacuation decisions: Hurricane Irma case study. *Transportation Research Part D: Transport and Environment*, 147, 104882. <https://doi.org/10.1016/j.trd.2025.104882>
- Ding, M., Zhou, H., Xie, H., Wu, M., Nakanishi, Y., & Yokoyama, R. (2019). A gated recurrent unit neural networks based wind speed error correction model for short-term wind power forecasting. *Neurocomputing*, 365, 54–61. <https://doi.org/10.1016/j.neucom.2019.07.058>
- Doury, A., Somot, S., Gadat, S., Ribes, A., & Corre, L. (2023). Regional climate model emulator based on deep learning: concept and first evaluation of a novel hybrid downscaling approach. *Climate Dynamics*, 60(5–6), 1751–1779. <https://doi.org/10.1007/s00382-022-06343-9>
- Esmalian, A., Wang, W., & Mostafavi, A. (2022). Multi-agent modeling of hazard–household–infrastructure nexus for equitable resilience assessment. *Computer-Aided Civil and Infrastructure Engineering*, 37, 1491–1520. <https://doi.org/10.1111/mice.12818>
- Fu, X., Li, H.-N., Tian, L., Wang, J., & Cheng, H. (2019). Fragility Analysis of Transmission Line Subjected to Wind Loading. *Journal of Performance of Constructed Facilities*, 33(5). [https://doi.org/10.1061/\(ASCE\)CF.1943-5509.0001311](https://doi.org/10.1061/(ASCE)CF.1943-5509.0001311)
- GB 50009-2012. (2012). Load Code for the Design of Building Structures. Beijing, China: China Architecture & Building Press.
- Han, S., Liu, B., Shi, C., Liu, Y., Qiu, M., & Sun, S. (2020). Evaluation of CLDAS and GLDAS Datasets for Near-Surface Air Temperature over Major Land Areas of China. *Sustainability*, 12(10), 4311. <https://doi.org/10.3390/su12104311>
- Han, T., Guo, S., Ling, F., Chen, K., Gong, J., Luo, J., Gu, J., Dai, K., Ouyang, W., & Bai, L. (2024). FengWu-GHR: Learning the Kilometer-scale Medium-range Global Weather Forecasting. *arXiv*.
- Harrowsmith, M., Nielsen, M., Jaime, C., Perez, E.C.D., Madhab Uprety, Homberg, M.V.D., Tijssen, A., Page, E.M., Lux, S., & Comment, T. (2020). Impact-Based Forecasting For Early Action The Future Of Forecasts. <https://doi.org/10.13140/RG.2.2.12366.89920>
- Huang, L., Gianinazzi, L., Yu, Y., Dueben, P.D., & Hoefler, T. (2024). DiffDA: a Diffusion Model for Weather-scale Data Assimilation. *arXiv*.
- Huang, X., & Wang, N. (2024). An adaptive nested dynamic downscaling strategy of wind-field for real-time risk forecast of power transmission systems during tropical cyclones. *Reliability Engineering & System Safety*, 242, 109731. <https://doi.org/10.1016/j.res.2023.109731>
- Huang, X., & Wang, N. (2025). Modeling probabilistic micro-scale wind field for risk forecasts of power transmission systems during tropical cyclones. *Structural Safety*, 116, 102620. <https://doi.org/10.1016/j.strusafe.2025.102620>
- Lam, R., Sanchez-Gonzalez, A., Willson, M., Wirnsberger, P., Fortunato, M., Alet, F., Ravuri, S., Ewalds, T., Eaton-Rosen, Z., Hu, W., Merose, A., Hoyer, S., Holland, G., Vinyals, O., Stott, J., Pritzel, A., Mohamed, S., & Battaglia, P. (2023). Learning skillful medium-range global weather forecasting. *Science*, 382(6676), 1416–1421. <https://doi.org/10.1126/science.adi2336>
- Leinonen, J., Nerini, D., & Berne, A. (2021). Stochastic Super-Resolution for Downscaling Time-Evolving Atmospheric Fields With a Generative Adversarial Network. *IEEE Trans. Geosci. Remote Sensing*, 59(9), 7211–7223. <https://doi.org/10.1109/TGRS.2020.3032790>
- Lim, J.-Y., Kim, S., Kim, H.-K., & Kim, Y.-K. (2022). Long short-term memory (LSTM)-based wind speed prediction during a typhoon for bridge traffic control. *Journal of Wind Engineering and Industrial Aerodynamics*, 220, 104788. <https://doi.org/10.1016/j.jweia.2021.104788>
- Liu, Z., Chen, H., Bai, L., Li, W., Chen, K., Wang, Z., Ouyang, W., Zou, Z., & Shi, Z. (2024). Deriving Accurate Surface Meteorological States at Arbitrary Locations via Observation-Guided Continuous Neural Field Modeling. *IEEE Transactions on Geoscience and Remote Sensing*, 62, 1–20. <https://doi.org/10.1109/TGRS.2024.3447073>
- Liu, Z., Chen, H., Bai, L., Li, W., Zou, Z., & Shi, Z. (2025). Kolmogorov Arnold Neural Interpolator for Downscaling and Correcting

- Meteorological Fields from In-Situ Observations. *arXiv*. <https://doi.org/10.48550/arXiv.2501.14404>
- Liu, Z., Lin, Y., Cao, Y., Hu, H., Wei, Y., Zhang, Z., Lin, S., & Guo, B. (2021). Swin Transformer: Hierarchical Vision Transformer using Shifted Windows. In *2021 IEEE/CVF International Conference on Computer Vision (ICCV)* (pp. 9992–10002). Montreal, QC, Canada: IEEE. <https://doi.org/10.1109/ICCV48922.2021.00986>
- Lu, X., Yu, H., Ying, M., Zhao, B., Zhang, S., Lin, L., & Bai, L. (2021). Western North Pacific Tropical Cyclone Database Created by the China Meteorological Administration. *Advances in Atmospheric Sciences*, 38(4), 690–699. <https://doi.org/10.1007/s00376-020-0211-7>
- Mara, T.G., & Hong, H.P. (2013). Effect of wind direction on the response and capacity surface of a transmission tower. *Engineering Structures*, 57, 493–501. <https://doi.org/10.1016/j.engstruct.2013.10.004>
- Mardani, M., Noah B., Yair C., Jaideep P., Chieh-Yu C., Cheng-Chin L., Arash V., Mohammad A.N., Tao G., Akshay S., Karthik K., Jan K., & Mike P. (2025). Residual corrective diffusion modeling for km-scale atmospheric downscaling. *Communications earth & environment*, 6(124). <https://doi.org/10.1038/s43247-025-02042-5>
- National Oceanic and Atmospheric Administration, National Weather Service. (2019). National hurricane center tropical cyclone report hurricane Michael.
- Olivetti, L., & Messori, G. (2024). Do data-driven models beat numerical models in forecasting weather extremes? A comparison of IFS HRES, Pangu-Weather and GraphCast. <https://doi.org/10.5194/egusphere-2024-1042>
- Perini De Souza, N.B., Sperandio Nascimento, E.G., Bandeira Santos, A.A., & Moreira, D.M. (2022). Wind mapping using the mesoscale WRF model in a tropical region of Brazil. *Energy*, 240, 122491. <https://doi.org/10.1016/j.energy.2021.122491>
- Price, I., Sanchez-Gonzalez, A., Alet, F., Andersson, T.R., El-Kadi, A., Masters, D., Ewalds, T., Stott, J., Mohamed, S., Battaglia, P., Lam, R., & Willson, M. (2025). Probabilistic weather forecasting with machine learning. *Nature*, 637(7959), 84–90. <https://doi.org/10.1038/s41586-024-08252-9>
- Rasp, S., Hoyer, S., Merose, A., Langmore, I., Battaglia, P., Russell, T., Sanchez-Gonzalez, A., Yang, V., Carver, R., Agrawal, S., Chantry, M., Ben Bouallegue, Z., Dueben, P., Bromberg, C., Sisk, J., Barrington, L., Bell, A., & Sha, F. (2024). WeatherBench 2: A Benchmark for the Next Generation of Data-Driven Global Weather Models. *Journal of Advances in Modeling Earth Systems*, 16(2), e2023MS004019. <https://doi.org/10.1029/2023MS004019>
- Reichstein, M., Benson, V., Blunk, J., Camps-Valls, G., Creutzig, F., Fearnley, C.J., Han, B., Kornhuber, K., Rahaman, N., Schölkopf, B., Tárrega, J.M., Vinuesa, R., Dall, K., Denzler, J., Frank, D., Martini, G., Nganga, N., Maddix, D.C., & Weldemariam, K. (2025). Early warning of complex climate risk with integrated artificial intelligence. *Nature Communications*, 16(1), 2564. <https://doi.org/10.1038/s41467-025-57640-w>
- Roy, K. C., Hasan, S., & Mozumder, P. (2020). A multilabel classification approach to identify hurricane-induced infrastructure disruptions using social media data. *Computer-Aided Civil and Infrastructure Engineering*, 35, 1387–1402. <https://doi.org/10.1111/mice.12573>
- Sekiyama, T.T., Hayashi, S., Kaneko, R., & Fukui, K. (2023). Surrogate Downscaling of Mesoscale Wind Fields Using Ensemble Superresolution Convolutional Neural Networks. *Artificial Intelligence for the Earth Systems*, 2(3), 230007. <https://doi.org/10.1175/AIES-D-23-0007.1>
- Skamarock, W.C., Klemp, J., Dudhia, J., Gill, D., Liu, Z., Berner, J., Wang, W., Powers, J., Duda, M., & Barker, D. (2019). A description of the advanced research WRF model version 4 (Vol. 145). National Center for Atmospheric Research.
- Ti, B., Li, G., Zhou, M., & Wang, J. (2022). Resilience Assessment and Improvement for Cyber-Physical Power Systems Under Typhoon Disasters. *IEEE Transactions on Smart Grid*, 13(1), 783–794. <https://doi.org/10.1109/TSG.2021.3114512>
- Tian, L., Zhang, X., & Fu, X. (2020). Fragility analysis of a long-span transmission tower–line system under wind loads. *Advances in Structural Engineering*, 23(10), 2110–2120. <https://doi.org/10.1177/1369433220903983>
- U.S Department of Energy, Infrastructure Security & Energy Restoration. (2018). Tropical cyclone Michael report 17.
- Wang, Z., Cun, X., Bao, J., Zhou, W., Liu, J., & Li, H. (2022). Uformer: A General U-Shaped Transformer for Image Restoration. In *2022 IEEE/CVF Conference on Computer Vision and Pattern Recognition (CVPR)* (pp. 17662–17672). New Orleans, LA, USA: IEEE. <https://doi.org/10.1109/CVPR52688.2022.01716>
- Weiss, A. (2001). Topographic position and landforms analysis. In Poster Presentation, ESRI User Conference, San Diego, CA.
- World Meteorological Organization (WMO). (2021). WMO Atlas of Mortality and Economic Losses from Weather, Climate and Water Extremes (1970–2019).
- Wu, B., Chen, W., Wang, W., Peng, B., Sun, L., & Chen, L. (2024). WeatherGNN: Exploiting Meteo- and Spatial-Dependencies for Local Numerical Weather Prediction Bias-Correction. *arXiv*. <https://doi.org/10.48550/arXiv.2310.05517>
- Wu, H., Zhou, H., Long, M., & Wang, J. (2023). Interpretable weather forecasting for worldwide stations with a unified deep model. *Nature Machine Intelligence*, 5(6), 602–611. <https://doi.org/10.1038/s42256-023-00667-9>
- Wu, Y., Wang, N., Huang, X., & Wang, Z. (2025). Enhancing power grid resilience during tropical cyclones: Deep learning-based real-time wind forecast corrections for dynamic risk prediction. *Reliability Engineering & System Safety*, 263, 111284. <https://doi.org/10.1016/j.res.2025.111284>
- Wu, Z., Pan, S., Long, G., Jiang, J., Chang, X., & Zhang, C. (2020). Connecting the Dots: Multivariate Time Series Forecasting with Graph Neural Networks. In *Proceedings of the 26th ACM SIGKDD International Conference on Knowledge Discovery & Data Mining* (pp. 753–763). Virtual Event CA USA: ACM. <https://doi.org/10.1145/3394486.3403118>
- Xiang, Y., Jin, W., Dong, H., Bai, M., Fang, Z., Zhao, P., Sun, H., Thambiratnam, K., Zhang, Q., & Huang, X. (2024). ADAF: An Artificial Intelligence Data Assimilation Framework for Weather Forecasting. *arXiv*. <https://doi.org/10.48550/arXiv.2411.16807>
- Xue, J., Mohammadi, F., Li, X., Sahraei-Ardakani, M., Ou, G., & Pu, Z. (2020). Impact of transmission tower-line interaction to the bulk power system during hurricane. *Reliability Engineering & System Safety*, 203, 107079. <https://doi.org/10.1016/j.res.2020.107079>
- Yang, S., Zhang, Y., Guo, T., Luo, M., Guo, J., & Ma, J. (2025). Rapid regional assessment of post-hazard structures and transportation infrastructure using aerial images. *Computer-Aided Civil and Infrastructure Engineering*, 40, 3833–3852. <https://doi.org/10.1111/mice.70015>

Zhong, X., Du, F., Chen, L., Wang, Z., & Li, H. (2024). Investigating transformer-based models for spatial downscaling and correcting biases of near-surface temperature and wind-speed forecasts. *Quarterly Journal of the Royal Meteorological Society*, 150(759), 275–289. <https://doi.org/10.1002/qj.4596>

Appendix A: Tower and Line Risk Mapping

A.1 Tower failure probability

This section formalizes the tower-level risk as a time-evolving probability of collapse driven by forecast wind loading. The formulation distinguishes between (i) the instantaneous, conditional failure probability at a given time step t , and (ii) the cumulative failure probability up to that time, accounting for survival in previous steps. The resistance R of a tower—its capacity against wind-induced collapse—is treated as an uncertain but time-invariant random variable over the forecast horizon (e.g., 12 h). Wind load S_t denotes the effective demand at time t obtained by mapping the wind speed (and wind attack angle) simulated by the ACDF to the positions of the transmission towers, and calculate the wind load distributed along the height of the transmission tower based on the wind-receiving area.

Independent failure probability. If one is only interested in the failure probability under a representative load level S (e.g., a peak or design wind state), the probability of failure P_f is given by the total probability with respect to resistance uncertainty:

$$\begin{aligned} P_f &= P(R < S) \\ &= \sum_{r \in R} P_{f|r} \cdot P(R = r), P_{f|r} = P(r < S) \end{aligned} \quad (\text{A1})$$

Cumulative probability up to time t . Over a forecast period τ with time-invariant resistance $R = r$,

$$\begin{aligned} P_{f,t} &= 1 - \sum_{r \in R} P(r \geq S_1, \dots, r \geq S_t) \cdot P(R = r) \\ &= \sum_{r \in R} P_{f,t|r} \cdot P(R = r) \end{aligned} \quad (\text{A2})$$

Assuming adjacent steps are statistically independent when the interval is several minutes (consistent with turbulence decorrelation under strong winds), the survival update for the conditional probability is:

$$P_{f,t|r} = P_{f,t-1|r} + (1 - P_{f,t-1|r})P'_{f,t|r} \quad (\text{A3})$$

where $P'_{f,t|r}$ is probability of tower collapse at time t only under load S_t conditional on $R = r$, which is the fragility function of the tower conditioned on a prescribed $R = r$. Then the $P_{f,t}$ becomes:

$$P_{f,t} = P_{f,t-1} + \sum_{r \in R} (1 - P_{f,t-1|r}) \cdot P'_{f,t|r} \cdot P(R = r) \quad (\text{A4})$$

These relations follow from the total probability theorem and the independence approximation at large time intervals (e.g., 10-min).

Fragility function for towers. The failure probability of the tower up to time t , $P_{f,t}$, can be estimated by using Monte

Carlo simulation (MCS) to sample tower resistance (r) from their predetermined distributions as previously discussed, then using fragility functions developed for different r values (i.e., $P'_{f,t|r}$) in each time segment for every sample realization. The detailed method of fragility functions development for transmission towers can be found in existing studies (Fu et al., 2019; Mara & Hong, 2013; Tian et al., 2020). For illustrative purpose in this study, all towers are assumed to be statistically independent and to share the same low-capacity fragility function, which is defined by a set of log-normal distributions $\Phi(\mu_\theta, \sigma_\theta)$ corresponding to different wind attack angles θ . The fragility function is defined as in Table A1.

Table A1. Fragility parameters by wind attack angle used in this study

Attack angle θ	0°	30°	45°	60°	90°
μ_θ	2.708	2.996	3.219	3.401	3.555
σ_θ	0.03	0.03	0.03	0.03	0.03

A.2 Line-level failure probability

A transmission line i is operationally unavailable if any of its supporting tower j collapses. This motivates a series-system abstraction in which the line fails when at least one tower fails:

$$P_{f,t}^{Line,i} = 1 - \sum_{\vec{r} \in \vec{R}} \prod_{j=1}^{n_i} (1 - P_{f,t|r_j}^{Tower,j}) \cdot P(\vec{R} = \vec{r}) \quad (\text{A5})$$

where tower j is the j th one in total n_i supporting towers of line i ; $P_{f,t|r_j}^{Tower,j}$, obtained by Equation A4, is the failure probability of tower j up to time t conditional on $R_j = r_j$; \vec{r} is the correlated samples for all n_i towers realized from the correlated tower resistances, \vec{R} , using MCS method.

A.3 Algorithmic workflow

The inputs and the end-to-end workflow used to convert ACDF wind forecasts into tower- and line-level failure probabilities suitable for operations are summarized as follows:

- **Wind fields:** 500 m resolution, hourly 10-m winds from ACDF over the forecast horizon.
- **Tower geolocation & orientation:** latitude/longitude for each transmission tower, plus line azimuth to compute wind-attack angle at the structure.
- **Line topology:** tower–line membership (series system abstraction: a line is down if any of its towers collapses).

- **Tower fragility and resistance:** angle-dependent lognormal fragility functions $P'_{f,t|r}$ that map wind load to instantaneous collapse probability, as defined in Table A1 in this study. These were developed with both load and resistance uncertainties considered during model development.

Let $t = 1, \dots, \tau$ index hourly forecast times.

Step 1. Interpolate the ACDF wind vector field to each tower location and decompose it relative to the line azimuth to obtain the attack angle. From wind speed and attack angle, compute the effective wind load on towers (GB 50009-2012, 2012; ASCE, 2015).

Step 2. Evaluate the instantaneous conditional failure probability at time t using the tower-specific fragility as defined earlier (see Equation A1). Update the cumulative (up-to-time- t) tower failure probability using the survival-update relation as defined earlier (see Equation A4).

Step 3. Treat each line as a series system of its supporting towers. Aggregate tower probabilities into a line-level failure probability using the complement-of-survival relation as defined earlier (see Equation A5).

Repeat Steps 1–3 for all $t = 1, \dots, \tau$. The survival update in Step 2 ensures monotonically non-decreasing tower probabilities over time; the series aggregation yields time-evolving line probabilities.